

MICRO/NANOENCAPSULATED PHASE CHANGE MATERIALS (PCMs)  
TOWARD HIGH TEMPERATURE  
THERMAL ENERGY STORAGE  
APPLICATIONS

*by*

HANFEI ZHANG

DISSERTATION

Submitted in partial fulfillment of the requirements  
for the degree of Doctor Philosophy at  
The University of Texas at Arlington

August, 2017

Arlington, Texas

Supervising Committee:

Shin, Donghyun (Advisor)  
Santhanagopalan, Sunand (Co-Advisor)  
Luo, Cheng  
Yum, Kyung Suk  
Moon, Hyejin

Copyright by  
Hanfei Zhang  
2017

## ACKNOWLEDGEMENTS

This work is supported by National Science Foundation Award # 1444473.

I would like to acknowledge the Characterization Center for Materials and Biology (C2MB) and Dr. Jiechao Jiang for providing the characterization equipment for this work.

A special thanks to my MuSES lab colleagues, Anirudh Balram, Bryan Steinhoff, who were constantly providing valuable suggestions and input to my work, and to MuSES lab alumni Dr. Ryan Lemmens for laying a solid foundation of this topic.

I would like to express the appreciation to Dr. Hani Tiznobaik for initial thermal analysis and Joohyun Seo for rheological tests.

I would also like to thank my dissertation committee members Dr. Cheng Luo, Dr. Hyejin Moon and Dr. Kyung Suk Yum who shared their insightful opinions about this work and helped make it better.

This work would not have been possible without the caring guidance of late Dr. Dennis Meng under whose tutelage I completed my masters' degree and began my PhD research.

I would like to especially thank my advisor Dr. Donghyun Shin whose thoughtful inputs helped me successfully complete my doctoral work.

Finally I would like to thank my advisor Dr. Sunand Santhanagopalan for the tremendous support of the idea development, insightful feedback on my work and the persistent commitment he displayed for this work. This work would not have been possible without his guidance.

## DEDICATION

This dissertation is dedicated to my beloved Shanshan Cui and little Sylvia, whose endless love and support always give me strength to keep looking forward, even throughout the toughest times.

I dedicate my work to my family, my parents Yi Zhang, Hong Wang and my parents in law Yuanhe Cui and Yaqin Wang, for their enthusiastic support provided to both my study and my life through the whole time. I also dedicate this work to my grandparents who always want to witness the completion of my doctoral study.

I am grateful to all my previous lab members from MTU and UTA, they all became my friends and helped me to build better understanding on academic life.

## ABSTRACT

### Micro/Nanoencapsulated Phase Change Materials (PCMs) toward High Temperature Thermal Energy Storage Applications

Hanfei Zhang, Ph.D.

The University of Texas at Arlington, 2017

*Supervising Professor(s): Shin, Donghyun; Santhanagopalan, Sunand*

Thermal energy is one of the most important renewable energy sources because of its abundance. However, despite the long history of people practically trying to harvest thermal energy, the efficiency of thermal energy storage and application to daily life utilization is still a major limitation, especially for high temperature (>300oC) applications. Concentrating solar power (CSP) is one of the very few technologies that have been used commercially to produce electricity from solar thermal energy. Benefiting from the extra latent heat stored during melting/freezing, phase change materials (PCMs) with a high melting point are commonly used in these systems functioning as thermal energy storage (TES) and heat transfer fluid (HTF). Further, to avoid contamination from surroundings and increase heat transfer rate, tremendous effort has been dedicated to make micro/nano-sized PCMs encapsulations. Yet, until now, most of the successful micro/nano-encapsulation techniques are not compatible with high temperatures due to the poor thermal/chemical stability of the capsules. A novel and cost effective modified sol-gel process was developed for the encapsulation of the first ever salt@silica microcapsules, which showed excellent thermal stability and reliability at high temperature. The encapsulation process was studied in detail and shown to be precisely controllable, demonstrated by different encapsulation ratios and shell thicknesses obtained. Rheological properties and thermal performance of microcapsules added HTF (solar salt) were then analyzed with the highest effective heat capacity enhancement of 11.0% obtained. Binary carbonate salt micro particles were then encapsulated via the same method. Through the high specific heat and latent heat of the binary carbonate salt, remarkable 40.5% and 134.4% enhancement on effective heat capacity over the best commercialized product was achieved respectively for active and passive solar thermal systems. Finally, the versatility of the developed encapsulation technique was demonstrated by micro/nano-encapsulation of different materials, along with the possibility of void creation.

## LIST OF FIGURES

Figure 1 Fabrication schematic .....	22
Figure 2 SEM images of a) ground KNO <sub>3</sub> particle; b&c) microencapsulation at different magnifications: concentration 1/1/20; d) X-ray mapping of S-1 microcapsules .....	24
Figure 3 SEM images of a) S-0.5 microcapsule; b) S-0.75 microcapsule; c) S-1.5 microcapsule; d) S-2 microcapsule. Left column figures are the x-ray mapping of the same particle in a).....	26
Figure 4 TEM images of hollow silica shell after dissolving of KNO <sub>3</sub> .....	27
Figure 5 FTIR comparison of a) S-2, KNO <sub>3</sub> and silica; b) samples with different TEOS concentration show different relative peak intensity between NO <sub>3</sub> <sup>-</sup> and Si-O-Si.....	29
Figure 6 Thermal analysis (2 <sup>nd</sup> DSC cycle). a) Stack of curves of KNO <sub>3</sub> salt and samples with different TEOS concentration; b) Melting and solidification of 2 <sup>nd</sup> DSC cycle of all samples; c) Plot of latent heat of fusion, encapsulation ratio and TEOS condensation efficiency; d) Thermal reliability of S-0.5, S-2 and KNO <sub>3</sub> over 10 DSC cycles. ....	32
Figure 7 SEM images of a, b, c) S-1 microcapsule after DSC at different magnifications; d) X-ray mapping of S-1 microcapsules after 10 cycles DSC test; e) FTIR comparison before and after DSC testing demonstrates retaining of chemical composition .....	37
Figure 8 SEM image showing morphology of a) as purchased KNO <sub>3</sub> crystal; b) hand ground KNO <sub>3</sub> @silica capsule; c) ball milled KNO <sub>3</sub> @silica capsule and d) particle size distribution of ground and ball milled sample.....	44
Figure 9 FTIR comparison of hand ground KNO <sub>3</sub> and ball milled KNO <sub>3</sub> .....	45

Figure 10 DSC analysis shows melting point depression and latent heat difference of a) 2 <sup>nd</sup> cycle of S-1.5 and S-BM1.5; b) 2 <sup>nd</sup> cycle of pure KNO <sub>3</sub> salt with different particle size.....	46
Figure 11 Effective heat capacity comparison among samples with different load .....	49
Figure 12 Viscosity of HTF (solar salt) with different sized microcapsules as additive at a range of temperatures. Each viscosity value at a specific temperature is an average of measurements at share rate from 100 s <sup>-1</sup> to 400 s <sup>-1</sup> .....	51
Figure 13 SEM imaging and x-ray mapping of LiK@Si capsule.....	57
Figure 14 FTIR comparison of LiK@Si, Li <sub>2</sub> CO <sub>3</sub> , K <sub>2</sub> CO <sub>3</sub> .....	57
Figure 15 DSC comparison of LiK@Si binary salt.....	59
Figure 16 Morphology of a) LiNa@Si microcapsules and b) Pure LiNa eutectic; c) X-Ray map of LiNa@Si and e)&f) particle size distribution of LiNa@Si .....	61
Figure 17 FTIR comparison of individual carbonate salts, LiNa binary salt, silica and LiNa@Si microcapsule .....	63
Figure 18 Latent heat of fusion for LiNa@Si-1.5, LiNa@Si-2 and the pure eutectic.....	65
Figure 19 Thermal reliability of LiNa@Si-1.5 and pure salt composite over 10 cycles .....	67
Figure 20 Latent heat values of 10 cycles for LiNa@Si-1.5 and Pure LiNa salt.....	68
Figure 21 X-ray maps of LiNa@Si-1.5 sample after 10-cycle DSC test.....	70
Figure 22 FTIR spectra of LiNa@Si-1.5 before and after 10-cycle DSC test.....	72

Figure 23 Effective heat capacity results of LiNa@Si and SS mixture at different load .....	75
Figure 24 Effective heat capacity of LiNa@Si for a passive hot tank storage .....	77
Figure 25 Effective heat capacity of K@S for a passive cold tank storage.....	78
Figure 26 Effective heat capacity comparison of LiNa@Si-1.5 and SS for passive 1-tank storage .....	80
Figure 27 SEM image and X-ray mapping of stainless steel encapsulated silica nanoparticles ..	83
Figure 28 Gallium@silica microencapsulation .....	84
Figure 29 SEM and TEM image of hollow silica nanoparticles.....	88
Figure 30 FTIR comparison of solid silica and mesoporous silica.....	90
Figure 31 Pore-plug sealing of porous shell after etching .....	92
Figure 32 BET surface area analysis of silica nanoparticles .....	95
Figure 33 Encapsulation of a&b) stearic acid and c) red phosphorous .....	96



# I Table of Contents

<b>I</b>	<b>TABLE OF CONTENTS .....</b>	<b>IX</b>
<b>II</b>	<b>GENERAL INTRODUCTION .....</b>	<b>11</b>
1.	BACKGROUND AND MOTIVATION .....	11
2.	GOALS FOR THIS WORK .....	14
<b>III</b>	<b>PROJECT DETAILS .....</b>	<b>16</b>
1.	CHAPTER I: MICRO-ENCAPSULATION OF MOLTEN SALT .....	16
1.1	<i>Introduction</i> .....	16
1.2	<i>Experimental</i> .....	20
1.3	<i>Results and discussion</i> .....	21
1.4	<i>Conclusion</i> .....	39
2.	CHAPTER II - EFFECT OF PARTICLE SIZE ON THERMAL PERFORMANCE IN HTF SYSTEM .....	40
2.1	<i>Introduction</i> .....	40
2.2	<i>Experimental</i> .....	42
2.3	<i>Results and discussion</i> .....	43
2.4	<i>Conclusion</i> .....	52
3.	CHAPTER III – THERMAL PERFORMANCE IMPROVEMENT: BINARY SALT MICROENCAPSULATION .....	53
3.1	<i>Introduction</i> .....	53
3.2	<i>Experimental</i> .....	54
3.3	<i>Results and discussion</i> .....	56
3.4	<i>Conclusion</i> .....	81
4.	CHAPTER IV: VERSATILITY OF THE ENCAPSULATION METHOD .....	82
4.1	<i>Stainless steel nanocapsules</i> .....	82

4.2	<i>Gallium microencapsulation</i> .....	84
4.3	<i>Hollow silica shell and void creation</i> .....	85
4.4	<i>Encapsulation of other materials</i> .....	96
4.5	<i>Conclusion</i> .....	97
<b>IV</b>	<b>FINAL CONCLUSION</b> .....	<b>98</b>
1.	PROJECT SUMMARY .....	98
2.	FUTURE WORK .....	100
<b>V</b>	<b>REFERENCES</b> .....	<b>101</b>
<b>VI</b>	<b>APPENDIX</b> .....	<b>107</b>
1.	LIST OF APPENDIX.....	107

## **II General Introduction**

### **1. Background and motivation**

Energy crisis has always been a concern throughout human history. Numerous efforts have been made to find available sources of energy. So far, fossil fuels are the most widely used and efficient source among them. Unfortunately, it is commonly accepted now that fossil fuel is approaching its depletion or will eventually become uneconomical to use thus should not be our only source of energy in the future. As technology advances, substitution or supplementation to fossil fuel needs to be explored, even though one ultimate solution is unlikely to be found in near future, quite a few have been picked and extensively studied. Thermal energy is one of them and will be an important energy form that human can rely on in the coming new era because of its abundancy and renewability. Thermal energy can be harvested from lots of sources like sun light, geothermal energy and waste heat generated by human activities, however, how efficiently thermal energy can be stored from those sources and transformed to daily life utilization is still questionable. To answer this question, thermal energy storage has been extensively studied to increase the working temperature and capacity of total energy stored. For different storing techniques, thermal storage can be categorized as sensible heat, latent heat and thermo-chemical heat storage, among which latent heat storage (LHS) draws the most attention from developers as it has better total heat capacity than sensible heat storage through utilizing of the latent heat of phase change materials (PCMs). For the moment, thermo-chemical heat storage is still considered at theoretical study stage.<sup>1</sup>

Concentrating solar power (CSP), as a practically operating power plant using renewable thermal energy, is one of the fields that high temperature PCMs are heavily involved. In CSP plants, the solar thermal energy is normally collected by parabolic mirrors or a central tower receiver to heat up a thermal storage material, then the thermal energy is carried through to a steam turbine by a heat transfer fluid or HTF to produce electricity. The high temperature associated with application expects the involved thermal energy storage materials to have high effective heat capacity and to be thermally and chemically stable in operation. One of the most mature technologies in CSP is active indirect 2-tank configuration where molten salt is pumping between the cold tank and hot tank serving as the thermal storage, while another HTF is heated and cooled by the molten salt through a heat exchanger and is circulating in the whole system. In order to increase the operation temperature, thus better efficiency for the Rankine cycle, a 2-tank direct configuration is established to use a single molten salt to work as thermal storage and HTF at the same time. This configuration does not require a heat changer hence reduces the cost and increased the overall efficiency of the system. However, due to the high freeze point of the HTF used (molten salt), auxiliary heat has to be supplied to the system during night hours to keep the system circulating. That being said, either a thermal storage material or a HTF with higher effective heat capacity is needed to improve the current CSP technology.

High temperature compatible MEPCM, with appropriate PCM material, has the potential to be incorporated with CSP in different ways to achieve aforementioned improvements. This work focuses on fabrication of micro encapsulated phase change materials (MEPCM) and its usage as a thermal storage material for high temperature applications.

As a sustainable thermal energy storage material, PCMs have been extensively studied because its thermal storage performance can benefit from the latent heat generated through the phase change. However at elevated temperature ( $>300^{\circ}\text{C}$ ), the choice of PCMs is limited to molten salt and metal/metal alloys, both of which have the issues of chemically unstable and corrosive to container at high temperature. Encapsulation is an effective solution to those aforementioned problems. Some efforts have been made for macro scale encapsulation, but to be used more efficiently, micro/nano-encapsulation is needed for PCMs. In addition, micro/nano sized capsules provide the benefits of easier handling and higher compatibility with different applications. Nevertheless, micro/nano-encapsulated PCMs has only been done for low-mid temperature application ( $T < 300^{\circ}\text{C}$ ), results from the using of polymers as the shell materials. It is widely known that the low-mid-grade heat only contribute to small amount of the waste heat generated by natural and human activities, a new method is needed to micro/nanoencapsulate PCMs for high temperature applications. This method should also be versatile such that it can be applied without much of material limitation.

## 2. Goals for this work

First chapter of this work is to propose a silica coating technique as the solution for micro/nano-encapsulation of molten salt towards high temperature applications. More specifically,  $\text{KNO}_3$  is encapsulated in silica shell using a cost effective sol-gel method. Other than proof of concept, different encapsulation ratios are also shown and characterized to demonstrate the controllability of the process. Thermal stability and thermal reliability tests are performed at a various temperature for these capsules with their thermal performance and chemical composition before and after test characterized.

In Chapter II, the effort has been made to obtain encapsulation with different particle sizes. A systematic study of as obtained salt (APS  $>100 \mu\text{m}$ ), hand ground salt (APS  $14 \mu\text{m}$ ) and ball milled salt (APS  $3 \mu\text{m}$ ) has been carried out with the samples' thermal performance characterized. The capsules with different size is then mixed with heat transfer fluid (solar salt), followed by the rheological and thermal analysis of the mixture with different sample load. As a proof of concept, effective heat capacity over a temperature range is also calculated for the MEPCM added HTF with different load.

Chapter III of this work is about encapsulating binary carbonate salts to achieve higher thermal energy storage capacity. Different binary salts, i.e. lithium - potassium/sodium carbonate has been encapsulated via the same method. This places our encapsulation into the application range of  $400 - 500^\circ\text{C}$  with a latent heat storage capability over  $200 \text{ J/g}$ . Characterization of encapsulation and thermal analysis is performed, with its thermal stability verified. Effective heat capacity is calculated based on different CSP

technologies and configurations, to demonstrate the phenomenal improvement over the current best thermal storage material.

Chapter IV of this work is about pushing the boundary of this encapsulation technique towards even higher temperature application and to show the versatility of the method, where metal/metal alloys (higher melting point), stearic acid (organic material), hollow sphere (versatility of fabrication) has been shown. Moreover, future direction of this encapsulation work has been discussed.

### **III Project Details**

#### **1. Chapter I: Micro-Encapsulation of Molten Salt**

##### **1.1 Introduction**

###### **1.1.1 Encapsulated PCMs**

Many organic and inorganic materials can be used as PCMs for the latent heat energy storage, but they all face different issues, including low thermal conductivity, poor thermal stability and causing corrosion to the container. In order to solve those problems, PCMs can be encapsulated in a shell material acting as a confinement or a “container” so that they are isolated from the surroundings. This shell material should have the properties of highly thermal conductive, thermo-chemically stable and should be able to accommodate the volume expansion during the phase change of the materials inside. Besides, the encapsulation should also allow the easy handling and transportation of the product, to make it suitable for different applications. Currently, most successful encapsulations are for low temperature applications, due to the difficulty of maintaining the thermo-chemical stability of the shell material at elevated temperature. Unfortunately, low grade heat is just a small portion of thermal energy that can be stored or reused. The waste heat generated by human activities has a wide temperature range and by nature higher grade heat has better efficiency when it is reused. Hence, there is great demanding of PCMs encapsulated thermal storage that can be incorporated into systems operates at mid-high temperature.



### 1.1.2 Low temperature encapsulations

For micro/nano-encapsulations, core materials have to be chosen in the consideration of their value of heat of fusion and compatibility with the encapsulation methods. However, concerning the maximization of energy storage efficiency, most of the micro/nano encapsulated PCMs have the drawback of only operating at low temperatures since the core materials normally have low melting points (i.e. paraffin wax, palmitic acid). There are other materials (i.e. molten salt) which have greater latent heat of fusion at higher phase change temperatures.<sup>2</sup> Salt nano-encapsulation has been reported previously. Graham et al. fabricated a salt hexahydrate core – polymer shell nanocapsule to benefit from the latent heat generated by hydration/dehydration of salt at around 90°C, again, for low temperature applications.<sup>3</sup> Besides, salt hydrates generally suffer great supercooling effect and low thermal stability.<sup>4</sup> For elevated temperature applications, thermal stability becomes a bigger issue and makes the polymer shell of current encapsulations unfavorable. A combination of high melting point core material and stronger, specifically thermo-chemically more stable, shell material is needed to fulfill the requirement of mid-high temperature thermal energy storage.

### 1.1.3 Material for high temperature application

Been called the Next-Gen thermal storage, high temperature encapsulations are badly needed for a lot of applications in industry.<sup>2</sup> Nomura et al. reported an Al-25 wt% Si core – Al<sub>2</sub>O<sub>3</sub> shell microcapsule to have a heat of fusion of over 240 J/g at 577°C. This is so far, to the best of author's knowledge, the only work concerning microencapsulated PCMs working at high temperature available. However, the boehmite coating and heat-

oxidation treatment used in aforementioned work, in order to create the shell on the surface of the core material, is not universally applicable for other materials. Actually, it is only available for the proposed aluminum silicon composite.<sup>5, 6</sup> As mentioned previously, molten salts are used for high temperature energy storage applications such like concentrated solar power (CSP) plant, a macroencapsulation of molten salt, proposed by Terrafore Inc., was reported to increase the energy density and reduces the cost of the power plant.<sup>7</sup> The work shows molten salt capsules with a high surface area that can increase the heat transfer rate. Also, a sacrificial polymer layer was incorporated in the capsule to create the void needed for accommodating the volume expansion during phase change. On the other hand, silica is a strong material for high temperature applications, because of its good thermo-chemical stability. In addition, nano-sized silica synthesis technique is widely available, such like sol-gel process via hydrolysis/condensation of alkoxide of silicon,<sup>8</sup> which makes silica an outstanding choice of shell material for micro/nano-encapsulation aiming for elevated temperature applications. Having that said, molten salt@silica core-shell structure can be a promising candidate to satisfy the requirements of next-gen thermal storage. Because of the wide range of the melting point of different salts, the salt encapsulations also have the opportunity for lots of other applications like thermal buffering of vehicle system.<sup>9</sup> However, there are technical barriers to make salt@silica capsules into micro and nano size. As silica condensation is normally done in an aqueous/organic solution in which most salts could not exist as separate form. To author's best knowledge there has no successful molten salt@silica micro/nano-encapsulation been reported for mid-high temperature applications to this point. So far silica has mainly been used to encapsulate low melting point PCMs such as

paraffin wax, n-octadecane and palmitic acid.<sup>10-13</sup> Indium silica nano-encapsulation has also been reported by Su et al. to have a latent heat of fusion of 16.6 J/g. The relevant low latent heat value is inherent in metals and metal alloys although they normally have a higher melting point. Technique modification is required to obtain salt/silica capsules.

Here author proposes a silica coating technique be used for micro/nano-encapsulation of molten salt for high mid-temperature applications. More specifically, this work is to present a successful attempt of making potassium nitrate and silica microencapsulation ( $\text{KNO}_3@$ silica) through a sol-gel process. Theoretically, this method can be used for most of the salt encapsulations at any size. Thermal stability and thermal reliability test are performed at a temperature of 400°C for these encapsulations with their thermal performance and chemical composition before and after test characterized. Finally potential application and future work are also discussed.

## 1.2 Experimental

As mentioned previously, salt microencapsulation has not been achieved because of the process compatibility issue. Here author propose a modified Stöber process for  $\text{KNO}_3$ @silica microencapsulation.<sup>8</sup> Hand ground potassium nitrate (Sigma Aldrich, 99%) was dispersed by an ultrasonic processor (Sonics & Materials, Inc.) in ethanol (Decon Labs, Inc., anhydrous) at 50% of power for 10 mins. Same weight of Polyvinylpyrrolidone (Sigma Aldrich) was added into the dispersion, and then the dispersion was constantly stirred for 24 hours to allow PVP to attach on the surface of  $\text{KNO}_3$  particles. Afterwards, PVP loaded  $\text{KNO}_3$  dispersion was centrifuged (Eppendorf 5702) to wash away the excessive PVP dissolved in the solution. Then fresh ethanol/ammonium hydroxide solution (Sigma Aldrich, 28%) mixture (1/0.04, v/v) was added into the dispersion followed by another 5 mins sonication to form a stable dispersion. Tetraethyl orthosilicate (TEOS) was finally added drop wise into the above dispersion by a syringe pump (New Era Pump Systems Inc.) at a speed of 2 ml/hour followed by a 1 hour condensation. The final concentration of  $\text{KNO}_3$ /TEOS/ethanol was kept at 1/x/20 (w/v/v, g/ml/ml) with the 'x' represents the different amount of TEOS used to obtain different encapsulation ratios. Constant stirring was applied during the whole process and the temperature of the dispersion was kept at 30°C. The product was collected by centrifuge and washed with water and ethanol after the condensation process, and then dried in ethanol at 50°C for 24 hours.

Field emission scanning electron microscopy (FESEM, Hitachi S-4800) and X-ray mapping was used to visualize the samples at different magnifications using an accelerating voltage of 20 kV. Samples with different encapsulation ratio were

characterized by Fourier transform infrared spectroscopy (FTIR, Thermo Nicolet 6700) and compared. Thermal analysis of all the samples were performed using differential scanning calorimetry (DSC Q20, TA Instruments)

### **1.3 Results and discussion**

#### **1.3.1 Coating Mechanism**

The fabrication schematic is shown in Figure 1. Silica encapsulating of PVP loaded solid material has been previously reported by Shi et al.<sup>14-16</sup> Different from the traditional method, water content in this process was limited and was solely from ammonia solution, with the intention of keeping solid form of salt.  $\text{KNO}_3$  solubility at this ethanol/water mixture is reported to be less than 0.1 wt% at 30°C from literature.<sup>17</sup> Silica is then readily formed on PVP coated  $\text{KNO}_3$  particles through the well-known Stöber process by drop wisely adding TEOS to the dispersion. The rate of hydrolysis and condensation of silica formation process is affected by the concentration of water, TEOS and ammonia.<sup>18-20</sup>

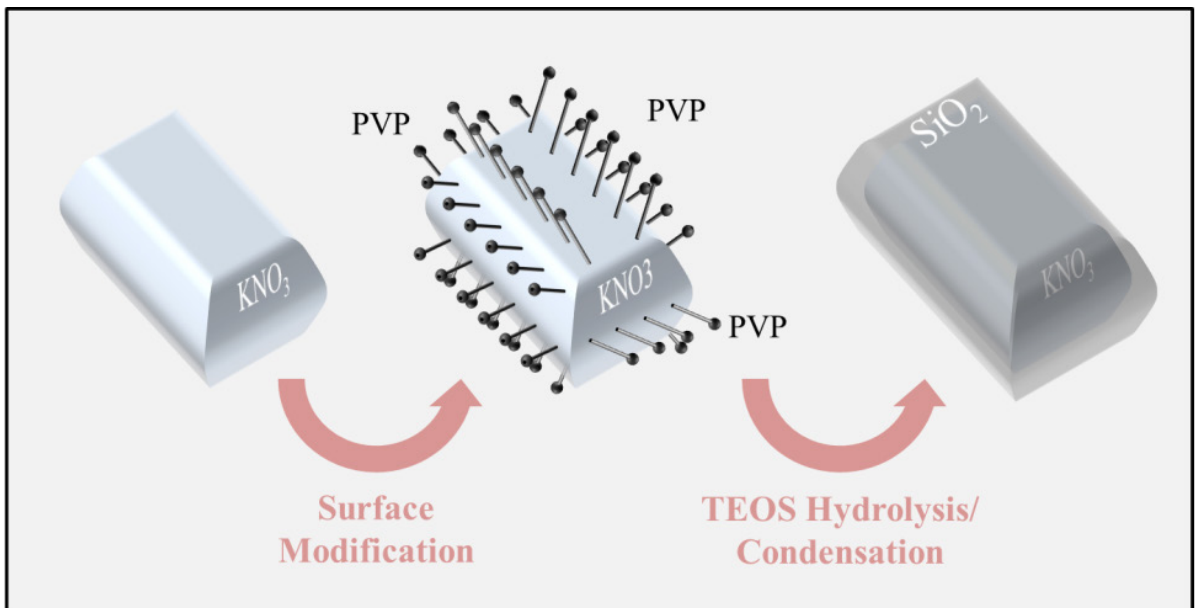


*Figure 1 Fabrication schematic*

### 1.3.2 Morphology characterization

Figure.2 shows the SEM images of  $\text{KNO}_3$ @silica microencapsulation. The concentration of  $\text{KNO}_3$ /TEOS/ethanol is 1/1/20 in this case and the capsule (Figure 2b) can be easily distinguished from the salt (Figure 2a) by visualization of the surface morphology. The particle size has a very wide distribution from several micrometers up to 20  $\mu\text{m}$ , due to the non-uniformity of hand grinding. An x-ray mapping (Figure 2 d) was also performed as an additional proof of encapsulation by showing the distribution of element Si, K and O. It is also noticed that there is no excessive silica particles forming around the microcapsules, indicates the process has sufficient surface area in the dispersion and fast hydrolysis and condensation rate. Previous study shows that secondary nucleation will happen when the critical surface area of silica seeds in the dispersion is not reached. In the meantime, maintaining a relatively short distance between seeds thus a short diffusion time for hydrolyzed TEOS monomers is also crucial to obtain monodispersed particles.

21-23

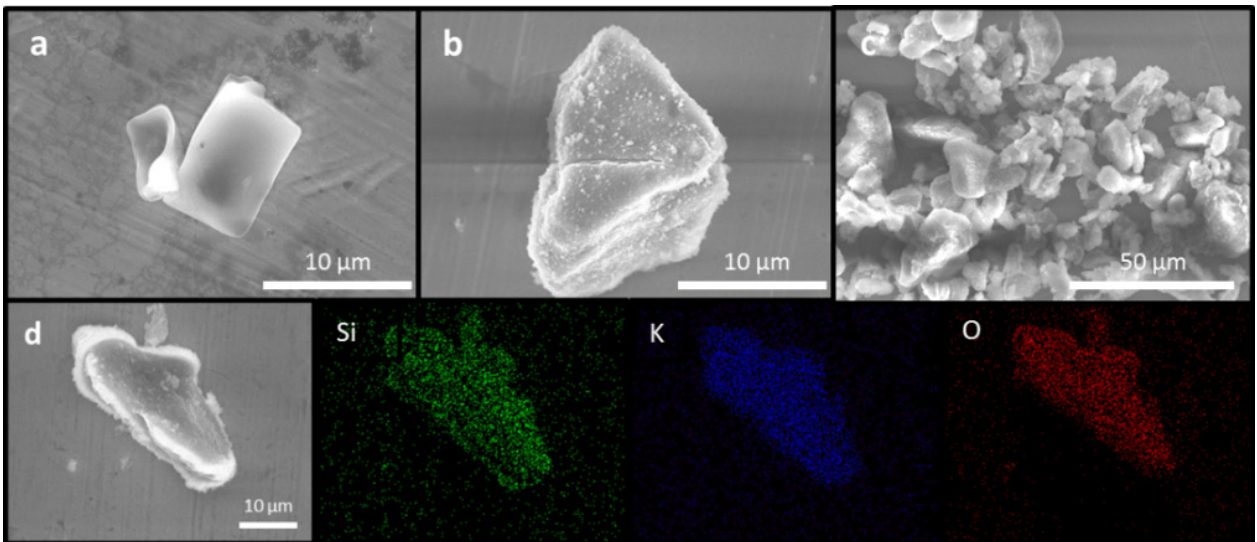


*Figure 2 SEM images of a) ground KNO<sub>3</sub> particle; b&c) microencapsulation at different magnifications: concentration 1/1/20; d) X-ray mapping of S-1 microcapsules*



### 1.3.3 Samples with different TEOS concentration

Different samples are obtained by varying the concentration of TEOS. The rest of the paper will use S-x for concentration  $1/x/20$ , for instance, S-1 is for sample with TEOS concentration of  $1/1/20$ . It is shown in Figure 3 that sample with different TEOS concentration has a different surface morphology, possibly attributable to the different hydrolysis and condensation rate. Higher TEOS concentration is reported to have a positive influence on hydrolysis / condensation rate and particle size.<sup>19</sup> From Figure 3 a-d, it is visually noticed the surface morphology of silica shell for different samples changes from smooth to rough when the TEOS concentration is increased. For S-0.5, the shell has a much lower condensation degree and is thin enough so that electron beam can penetrate and imagine the salt within the capsule (Figure 3 a). This observation is supported by an X-ray map of the same particle (Figure 3 left column), in which the distribution of K and Si element matches with the SEM image. Furthermore, a smooth but non-transparent shell is observed in S-0.75 (Figure 3 b), while the coating is getting rough and bumpy for samples with higher TEOS concentration (i.e. S-1.5 and S-2, Figure 3 c-d). Author believes that small primary particle size and low condensation degree of silica, both of which are resulted from low TEOS concentration, are the causes of the smooth thin shell formation. More SEM images and X-Ray mappings for samples with different TEOS concentration can be found in Appendix 1. Additionally, the shell thickness of S-0.75 and S-1.5 sample can be approximated from the TEM image after salt had been dissolved from the sample during sonication in water, where empty shell can be visualized. The shell thickness is approximately  $\sim 130$  nm and  $\sim 60$  nm for S-1.5 and S-0.75 respectively (Figure 4).

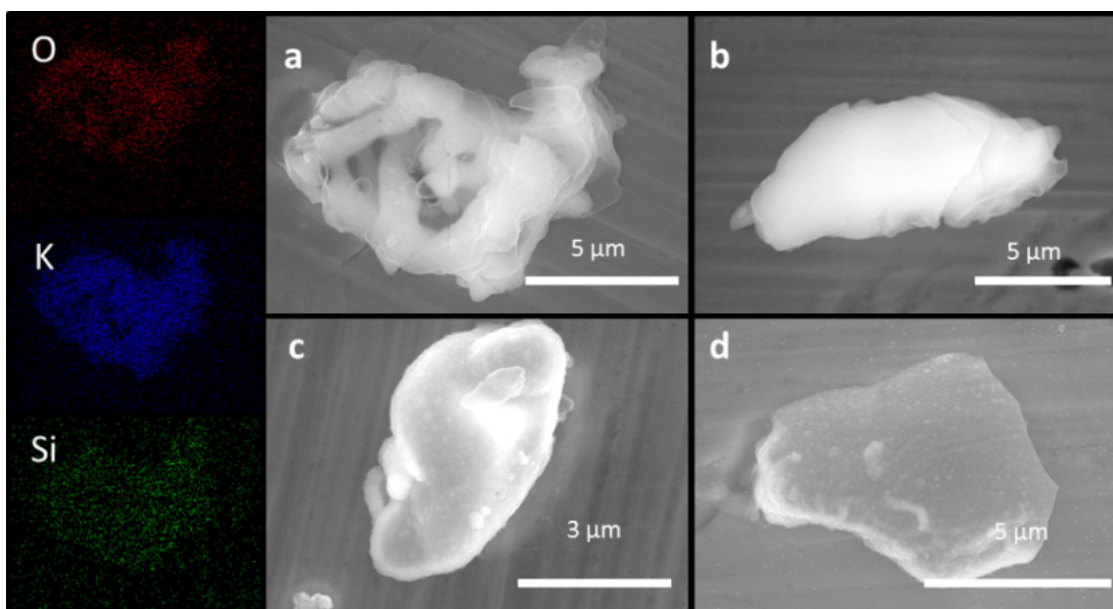


*Figure 3 SEM images of a) S-0.5 microcapsule; b) S-0.75 microcapsule; c) S-1.5 microcapsule; d) S-2 microcapsule. Left column figures are the x-ray mapping of the same particle in a)*

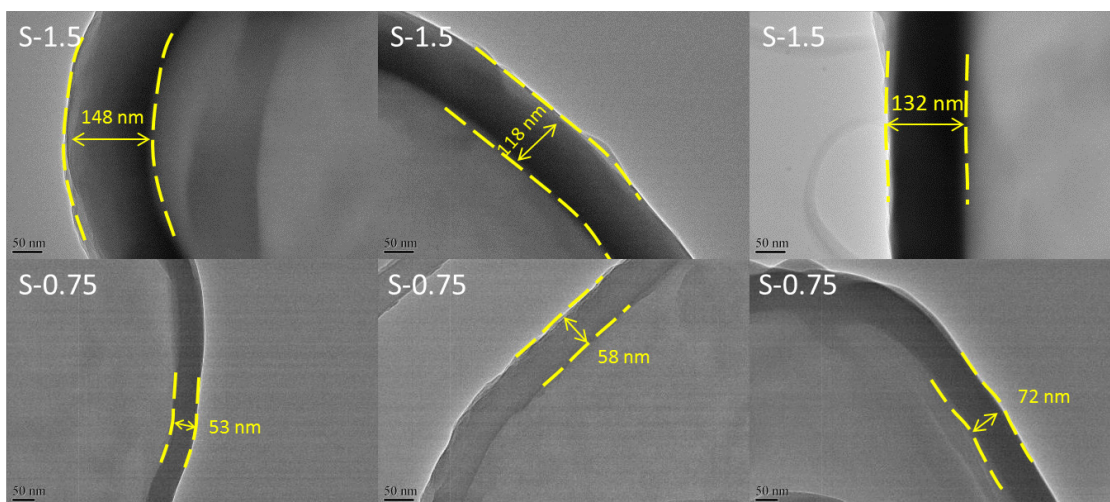


*Figure 4 TEM images of hollow silica shell after dissolving of  $KNO_3$*

#### 1.3.4 FTIR before DSC

FTIR was recorded to characterize the chemical composition of the encapsulation and to demonstrate the controllability of the process. There is a clear presence of  $\text{NO}_3^-$  symmetric bending band,  $\text{NO}_3^-$  asymmetric stretching band and Si-O-Si asymmetric stretching band at  $825\text{ cm}^{-1}$ ,  $1373\text{ cm}^{-1}$  and  $1072\text{ cm}^{-1}$  respectively in  $\text{KNO}_3@\text{silica}$  sample, indicates the encapsulation has preserved the chemical properties of the raw materials (Figure 5 a).<sup>24-26</sup> Among the samples, the increasing peak intensity ratio between N-O and Si-O-Si bond is also observed for a decreasing TEOS concentration (Figure 5 b), demonstrating lesser silica formation at lower TEOS concentrations.

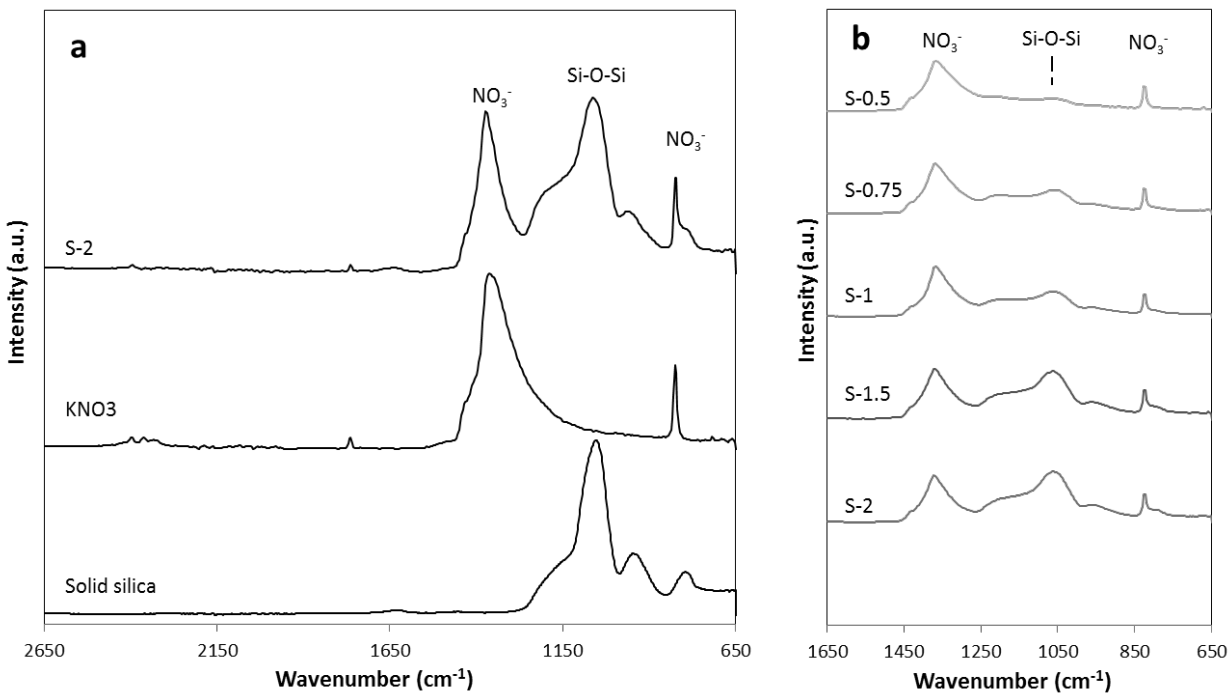


Figure 5 FTIR comparison of a) S-2, KNO<sub>3</sub> and silica; b) samples with different TEOS concentration show different relative peak intensity between NO<sub>3</sub><sup>-</sup> and Si-O-Si

Differential scanning calorimetry (DSC) was used to characterize the heat storage performance and thermal stability of the samples. The microcapsules were subjected to 10 cycles of heating/cooling ramp from a temperature range of 40°C to 400°C, resulted a good latent heat recovery and thermal stability, moreover, our capability of controlling encapsulation ratio and encapsulation efficiency was also demonstrated.

#### 1.3.5 Phase change characteristics

The second cycle from DSC test of raw  $\text{KNO}_3$  and samples with different TEOS concentration are stacked together to illustrate the resemblance of their thermal performance (Figure 6a). The two exothermic and endothermic peaks at around 130°C, come from the hydration/dehydration of  $\text{KNO}_3$  hydrate, represent melting/solidifying latent heat of the salt hydrate.<sup>4</sup> These two peaks and the latent heat they stored are not an interest of this work due to their presence at relatively low temperature. Instead, the other two major peaks appeared at the phase change temperature of  $\text{KNO}_3$ , around 334°C, are the main focus of the thermal analysis. A magnified view of the melting/solidifying peak of different samples is shown in Figure 6b. The raw  $\text{KNO}_3$  and the microcapsules have relatively the same peak position and melting/solidifying behavior, indicates the decent preservation of the physical property of the salt, which is essential for a successful PCM encapsulation. It is also noticed that there is a small onset of melting and solidifying depression for the encapsulated samples, which is widely observed for micro/nanoencapsulations by other researchers. However, the causing of melting depression and solidifying depression may be different. Melting point depression is normally explained in literature by interfacial free energy differences between solid/wall and liquid/wall and impurity caused entropy change,<sup>11, 27-31</sup> while in this case, the

solidifying point depression hypothetically can be more accurately described by the negative pressure generated from the thermal contraction mismatch between silica and molten  $\text{KNO}_3$  salt, as well as the detachment of liquid from crystallization nucleation site,<sup>32</sup> in this case, the capsule wall. Nevertheless, the significant supercooling amplifying effect been reported previously in TEOS derived indium/silica nano-encapsulation, due to non-wetting interface between indium/silica caused homogeneous nucleation,<sup>28</sup> is not observed in this case. The supercooling for the thermal cycle (measured as the difference between finishing temperature of melting and solidifying peaks for a better representation of a thermal loop) of raw  $\text{KNO}_3$ , S-0.5 and S-2 are  $16^\circ\text{C}$ ,  $16^\circ\text{C}$  and  $19.81^\circ\text{C}$  respectively. The  $3.81^\circ\text{C}$  incremental supercooling can be considered a small change compare to other TEOS derived micro/nano-encapsulation.<sup>28</sup>

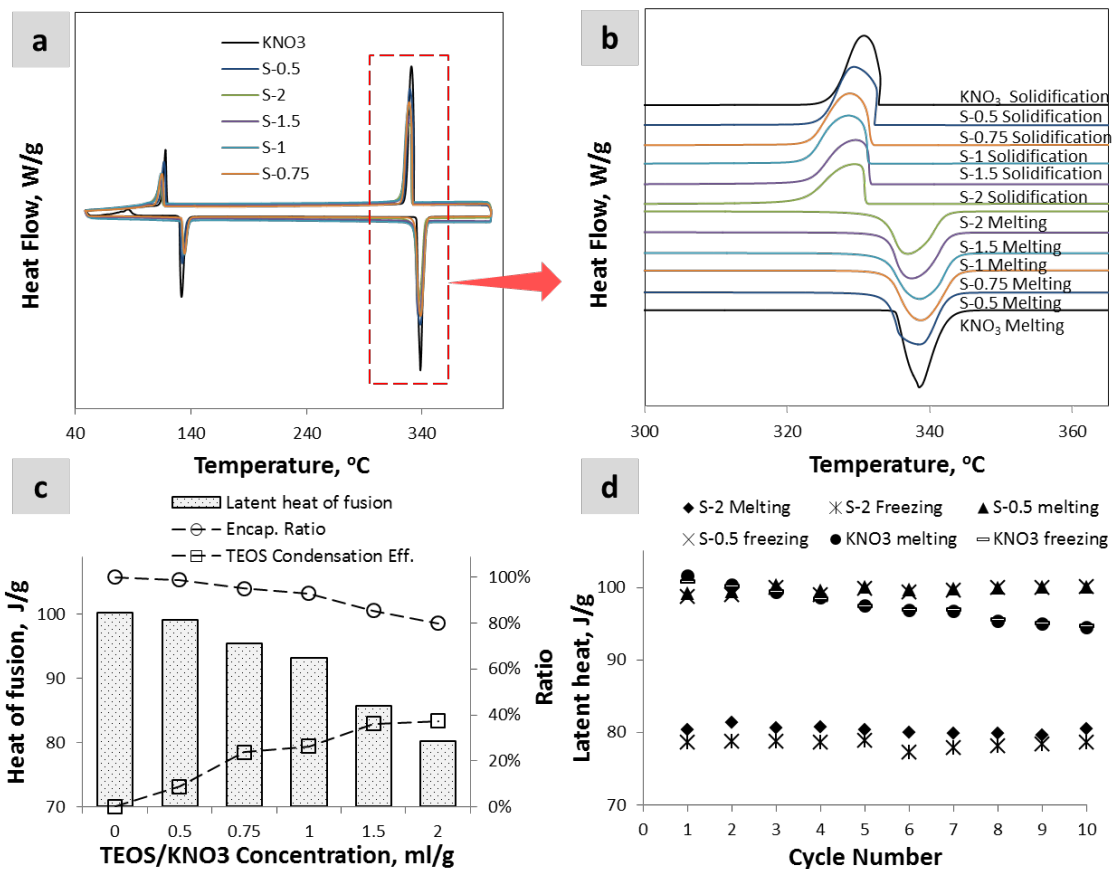


Figure 6 Thermal analysis (2<sup>nd</sup> DSC cycle). a) Stack of curves of KNO<sub>3</sub> salt and samples with different TEOS concentration; b) Melting and solidification of 2<sup>nd</sup> DSC cycle of all samples; c) Plot of latent heat of fusion, encapsulation ratio and TEOS condensation efficiency; d) Thermal reliability of S-0.5, S-2 and KNO<sub>3</sub> over 10 DSC cycles.



### 1.3.6 Latent heat and reliability

To evaluate the thermal storage performance of the microcapsules, the latent heat of fusion and crystallization are obtained by integrating the heat flow data (Universal analysis 2000, TA Instruments) of the melting and solidifying peaks. The results show that the microcapsules recover the latent heat very well. Moreover, the TEOS concentration now can be coupled with encapsulation ratio, finally demonstrates the excellent control of the encapsulation process, which enables the managing of tradeoff between heat storage performance and thermal stability by changing the core-shell composition in the microcapsule. In terms of heat of fusion, S-0.5 has the highest value of 99.13 J/g with the encapsulation ratio of 98.8% (however, it failed the thermal stability test, details of which will be discussed in next section). Meanwhile, S-2 has the lowest heat of fusion of 80.17 J/g with an encapsulation ratio of 77.04%. Incremental silica content is accountable for the decreasing of latent heat in samples with lower encapsulation ratio. Rest of the values is shown in Figure 6c and Table.1. Furthermore, thermal reliability test shows latent heat is recovered well within the 10 cycles (Figure 6d). Degradation on thermal performance of raw  $\text{KNO}_3$  has already been observed even within 10 cycles, while the latent heat remains almost the same for both S-0.5 and S-2 microcapsules, of which the reasons of this enhanced thermal reliability may be explained differently. It is hypothesized that the good thermal reliability of S-2 microcapsules comes from the prevention of degradation and phase segregation of the salt provided by the encapsulation, at the same time, a noticeable separation between latent heat values of melting and solidification is observed, which has been commonly reported for micro/nano-encapsulations.<sup>5, 12</sup> It is likely that the sample was still stabilizing

at first 10 cycles, so that small fluctuation on latent heat value is detected. On the other hand, S-0.5 microcapsule also maintained, with a little improvement, on the latent heat, however, the microcapsules after thermal cycling is observed to be completely damaged (SEM images are shown in Appendix 2 and details will be provided in a following section), therefore the stable latent heat recovery has to be attributed to other reasons. Silica nanoparticle additive in KNO<sub>3</sub> salt matrix is reported to give an enhanced heat of fusion.<sup>33</sup> In this case, the stable or slightly enhanced latent heat of S-0.5 sample over cycles is suspected to result from the broken silica shells, which could act as an additive within the sample. A DSC result comparison of 10 cycles of S-0.5 and S-0.75 has been provided in Appendix 3 to show the deviancy of melting peaks of S-0.5 during test while the peaks of S-0.75 remain similar to each other. Additionally, the small or unnoticeable separation between latent heat of melting and solidification also shows the S-0.5 sample behaves differently from an encapsulation (i.e. S-2) during the test. Detailed result of 10 cycles of melting/solidification DSC data of all samples is provided in Appendix 4.

*Table 1 Thermal analysis results*

Sample	Heat of fusion (J/g)	Heat of freezing (J/g)	Encapsulation Ratio (%)	Encapsulation Eff. E (%)	Silica w%	TEOS condensation efficiency
KNO3	100.3	100	100	100	0	n/a
S-0.5	99.13	98.78	98.8	98.8	1.17%	8.60%
S-0.75	95.48	92.97	95.2	94.1	4.81%	23.80%
S-1	93.19	91.46	92.9	92.2	7.09%	26.30%
S-1.5	85.67	82.89	85.4	84.2	14.59%	36.10%
S-2	80.17	77.04	79.9	78.5	20.07%	37.30%

### 1.3.7 Encapsulation characteristics

It should be mentioned that below calculation involves some error since the cooling rate was not controllable by the DSC instrument. Encapsulation ratio (R) and encapsulation efficiency (E) are important indications of the encapsulations. They are calculated for KNO<sub>3</sub>@silica microcapsules as below:

$$R = \frac{Q_{m,capsule}}{Q_{m,salt}} \times 100\% \quad \text{----- (1)}$$

$$E = \frac{Q_{m,capsule} + Q_{f,capsule}}{Q_{m,salt} + Q_{f,salt}} \times 100\% \quad \text{----- (2)}$$

Where  $Q_{m,capsule}$  and  $Q_{f,capsule}$  are the heat of fusion and heat of crystallization for microcapsule respectively, while  $Q_{m,salt}$  and  $Q_{f,salt}$  are the according values for raw KNO<sub>3</sub> salt. The inverse correlation between encapsulation ratio and TEOS concentration is expected and successfully observed, demonstrates the extraordinary controllability of the encapsulation process. It is clearly shown in Table.1 that encapsulation efficiency decreases with increased TEOS concentration, which again is exactly the trend we expected to demonstrate here. However, a tradeoff between high efficiency and good thermal stability needs to be made. Silica (as the shell material) has a direct impact on the gravimetric thermal storage performance, therefore, an ideally thin coating, yet is strong enough to accommodate salt volume change during thermal cycling, is needed for performance optimization. Thus understanding the TEOS condensation behavior in this process is crucial. The term TEOS condensation efficiency is used here to represent how efficiently TEOS can be converted to silica in comparison of different starting concentrations. TEOS condensation efficiency is obtained by firstly calculating silica

weight percentage in the microcapsule mathematically from the encapsulation ratio as  $1-R$ , followed by comparing this actual weight to the maximum weight can be obtained if all TEOS converts to silica. The results are shown in Table.1. Although silica weight percentage follows the anticipated trend and increases with increased TEOS concentration, i.e. S-0.5 has a wt% value of 1.17% while it is 20.07% for S-2, TEOS condensation efficiency behaves less linearly and presumably is going to reach a limit at higher starting concentration (Table.1 & Figure 6c). An incremental TEOS condensation efficiency difference of 17.7% and 9.8% is observed from S-0.5 to S-1 and from S-1 to S-1.5 respectively, while only 1.2% incremental can be obtained from S-1.5 to S-2. This concentration limited effect agrees with a previous report about Stöber sol-gel process, where a maximum silica yield percentage was reached at a particular TEOS concentration, after which ammonia concentration became the limiting factor of silica growth.<sup>34</sup>

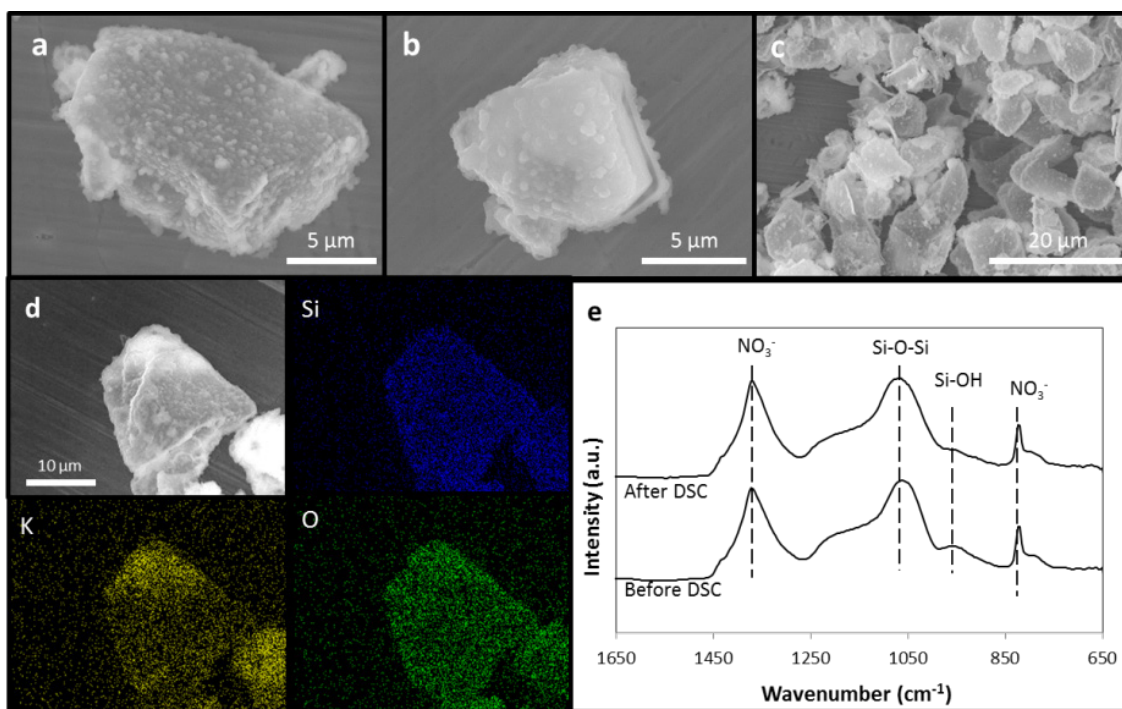


*Figure 7 SEM images of a, b, c) S-1 microcapsule after DSC at different magnifications; d) X-ray mapping of S-1 microcapsules after 10 cycles DSC test; e) FTIR comparison before and after DSC testing demonstrates retaining of chemical composition*

### 1.3.8 Thermal stability

Samples after DSC test are re-dispersed in ethanol and imaged by SEM for thermal stability characterization. As mentioned above, although S-0.5 sample has the highest latent heat recovery and encapsulation efficiency (98.8%), the failing of its thermal stability test makes it undesirable for practical applications. Thus the next best encapsulation efficiency obtained is 94.1% for S-0.75, which has passed the reliability test. In Appendix 2, the SEM image of S-0.5 sample after 10 cycles of DSC test shows no sign of microcapsule, instead, lots of similarly shaped salt crystals, recrystallized from the dispersion solution during SEM sample preparation, are found, indicates shell breakage and exposure of  $\text{KNO}_3$  after DSC test. This statement is also supported by the TEM image of S-0.5 samples after the salt been washed away during sonication, where broken hollow silica shells can be clearly observed from the images (Appendix 5). By contrast, SEM images of S-1 after DSC sample are taken at different magnifications (Figure 7a, b, & c) to visualize the intact microcapsules after thermal cycling. Other than the morphology, chemical composition is also retained after thermal cycling, illustrated by an x-ray map of S-1 microcapsule after DSC (Figure 7d) and a FTIR comparison of sample before and after DSC test (Figure 7e). The FTIR peak intensity reduction at  $957\text{ cm}^{-1}$  indicates the higher condensation degree of silica after DSC test due to the loss of Si-OH bond at high temperature thermal cycling. It is also noticed there that there is a small red shift of Si-O-Si bond from  $1072\text{ cm}^{-1}$  to  $1076\text{ cm}^{-1}$  possibly indicating a more opened structure on the shell after the thermal cycling at the elevated temperature.<sup>15, 16</sup> The outstanding thermal stability of the  $\text{KNO}_3@$ silica microcapsules is additionally proved by the retaining of the samples' powder form after DSC test, illustrated by photos

taken after DSC (Appendix 6), where raw  $\text{KNO}_3$  salt and exposed  $\text{KNO}_3$  salt from broken capsule (S-0.5) results sticky paste after test. The slightly darker color of samples with higher TEOS concentration is a result of carbonization of uncondensed ethyl group in silica network at the low oxygen environment in DSC test.

#### **1.4 Conclusion**

A  $\text{KNO}_3@$ silica microencapsulation is reported first time for high temperature applications with excellent thermal reliability and stability for 10 heating/cooling cycles. The versatile water-limited sol-gel silica coating method can theoretically be used for any salt PCMs encapsulation at micro/nano scale, achievement of which has not been reported in the past. This broadly opens the opportunities for scalable and cost effective fabrication of micro/nanoencapsulated PCMs for high temperature applications. Furthermore, great controllability on shell formation and encapsulation ratio has also been demonstrated in current work, from where, optimization like PCM selection, application temperature, particle size and thermal performance can be performed in the future.

## 2. Chapter II - Effect of Particle Size on Thermal Performance in HTF System

### 2.1 Introduction

Microencapsulated phase change materials (MEPCM) have received considerable attention recently because they have better heat conductivity and are environmentally more friendly than macroencapsulated PCMs and exposed PCMs when they are incorporated to different media like building and heat transfer fluid.<sup>35-41</sup> MEPCM slurry, utilizing the latent heat of PCM to increase the heat capacity of the heat transfer fluid (HTF), has been studied intensively by researchers,<sup>35, 37, 38, 40, 42, 43</sup> however, most of the existing work is for low temperature working fluid such like water.<sup>39, 40, 44</sup> This is mainly because of the lack of high temperature compatible MEPCM. The shell of the current microcapsules, typically polymer, is not thermally stable for the high temperature applications (over 300°C).<sup>45</sup> As a result, a MEPCM slurry working at high temperature, which is essential to applications using high temperature heat transfer fluid such like concentrated solar power (CSP) plant,<sup>46</sup> has not been established and studied. This work aims to synthesize novel microencapsulated PCMs capsules that can be made into high temperature heat transfer fluid, and to study its enhanced thermal performance.

Depending on the size of the capsule, encapsulated PCMs are categorized as Macroencapsulated PCMs (capsule size larger than 1 mm), Microencapsulated PCMs (capsule size between 1  $\mu$  m to 1000  $\mu$  m) and Nanoencapsulated PCMs (capsule size less than 1000 nm). Macroencapsulated PCMs focused on mid-high temperature applications are previously investigated for some experimental purposes in industry.<sup>7, 47,</sup>

<sup>48</sup> Terrafore proposed a macro scale nitrite salt core – inorganic shell structure for



concentrating solar power (CSP) plant application. A sacrificial polymer layer was used to create a gap between shell and core material to accommodate the thermal expansion;<sup>7</sup> Zheng et al. used stainless steel and carbon steel as shell material for binary salt encapsulation;<sup>47</sup> More recently, Nomura et al. used metal core-ceramic shell configuration to take advantage of the high thermal conductivity of metal as core material.<sup>48</sup> Compared to macro capsules, micro-encapsulation and nano-encapsulation have the all the benefits of becoming small such as much higher surface area (better heat transfer), better mechanical properties and better versatility in terms of application, i.e. they can be integrated with various systems like building walls and heat transfer fluids (HTF) to give enhanced thermal properties to those systems. However, micro and nano-encapsulation are much more selective on materials because most of them are made from wet chemistry process. For instance, micro-encapsulation is normally done by in-situ polymerization and interfacial polymerization methods.<sup>10, 13, 49-54</sup> One of the widely used core materials is paraffin wax. Its wide melting point range, high specific heat capacity and heat of fusion make paraffin wax a popular phase change material for low temperature applications<sup>13, 52, 55-57</sup>. There are also work reported for microencapsulation of n-Octadecane,<sup>10</sup> alkaline salt hydrate,<sup>58</sup> hexadecane,<sup>59</sup> etc. Typically, polymers are used as the shell materials for micro-encapsulation, although silicon dioxide and titanium dioxide are also reported.<sup>10, 13, 52</sup> For nano-encapsulation, similar techniques are used along with some other methods such as emulsion polymerization and sol-gel methods. Paraffin wax, palmitic acid, n-Dodecanol and n-Octadecane are previously reported as the core material.<sup>11, 12, 49, 50, 60-67</sup> However, as mentioned previously, micro/nano-

encapsulation for high temperature application is rarely achieved because of the poor process compatibility.

## 2.2 Experimental

$\text{KNO}_3$ @silica microcapsules were synthesized in-house. Capsules with different particle size were obtained by using different milling methods. Commercially received potassium nitrate (Sigma Aldrich, 99%) was firstly ground in a mortar. As obtained powder was functionalized with polyvinylpyrrolidone (PVP, Sigma Aldrich) then washed with ethanol to remove the excessive surfactant in dispersion. Finally the core-shell structure was obtained by coating silica around the salt particles via a water-limited silica coating process. Specifically, PVP loaded  $\text{KNO}_3$  particles were dispersed in an ethanol/ammonia (v/v 1/0.04) solution, followed by a dropwise injection of tetraethyl orthosilicate (TEOS, Sigma Aldrich) to initiate the sol-gel process. The final concentration of chemicals used in this sol solution is 1/1.5/20,  $\text{KNO}_3$ (g)/TEOS(ml)/Ethanol(ml). The sol solution was then stirred for another hour at 30°C. As synthesized microcapsules were obtained by centrifuging the sol-gel dispersion and then washed with water and ethanol to remove any remaining chemicals. To obtain a microcapsule with different size, as purchased  $\text{KNO}_3$  powder was ball milled (SPEX SamplePrep, Mixer/Mill) in stainless steel 304 vials for 30 minutes before the PVP loading.

Field emission scanning electron microscopy (FE-SEM, Hitachi S-4800) was used to visualize the morphology of the capsules. Differential scanning calorimetry (DSC Q20, TA Instruments) was used to measure latent heat and thermal reliability/stability. 1%, 5%

and 10% weight percentage of as synthesized micro capsules were mixed with solar salt respectively for viscosity testing using a rheometer.

## **2.3 Results and discussion**

### **2.3.1 Morphology and particle size analysis**

A novel water-limited silica coating technique based on Stöber process is used to synthesize the molten salt@silica microcapsules.<sup>8, 15</sup> This method, with much lower or no limitation on core materials (PCMs) selection comparing to previously reported method,<sup>5</sup> overcomes the incompatibility issue between water based silica microencapsulation process and water soluble molten salt. The encapsulation ratio (core/shell composition) can also be easily controlled by varying the KNO<sub>3</sub> and TEOS ratio. From Figure 8a, it is noticed that as purchased KNO<sub>3</sub> particles have a shining surface (because of the charging under electron beam in FE-SEM), while the microcapsules (Figure 8b) shows a continuous coated surface without much of charging effect, which indicates the presence of the silica shell. An x-ray mapping of the microcapsule is also provided in previous chapter to visualize the distribution of the elements, which exactly demonstrates the obtained microcapsule has a core-shell structure.

From Figure 8, clear size difference can be observed from SEM images of as purchased salt, hand ground capsule and ball milled capsule. ImageJ was used for the particle size analysis of the latter two. As seen in Figure 8d, ball milled KNO<sub>3</sub>@silica (S-BM1.5) capsules has a APS of 3.6(±2.1) nm, while hand ground sample has a much bigger average particle size with a wide distribution (APS 14.1 (±7.4) nm)

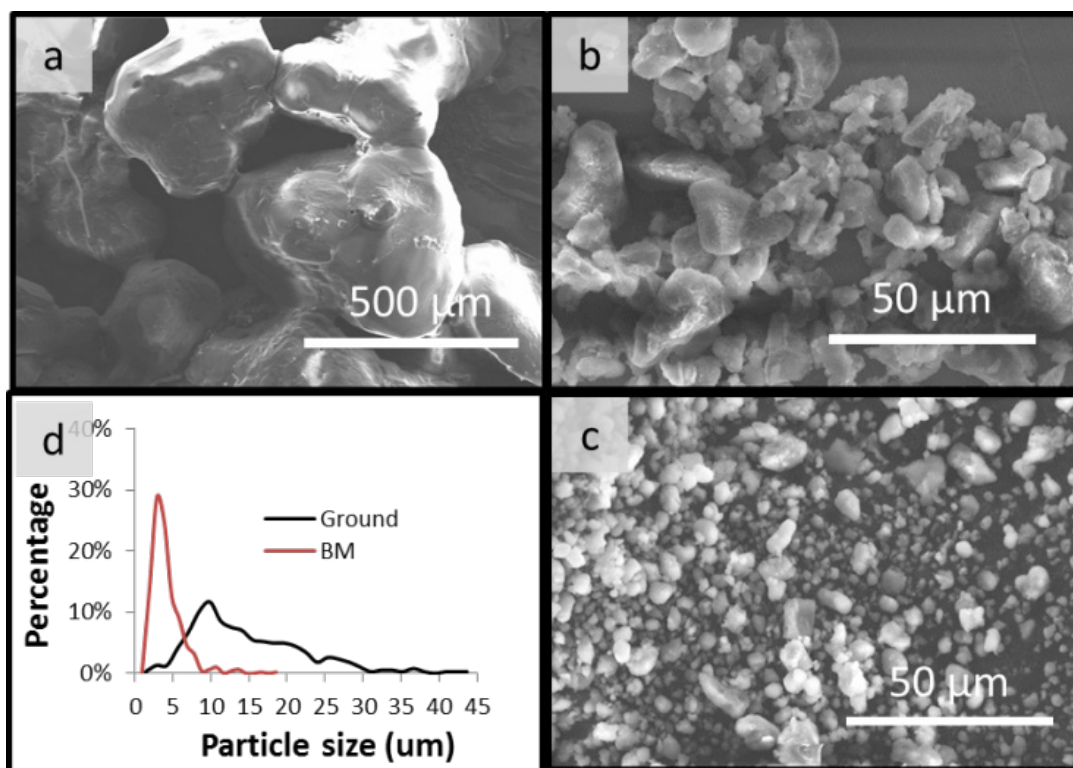


*Figure 8 SEM image showing morphology of a) as purchased KNO<sub>3</sub> crystal; b) hand ground KNO<sub>3</sub>@silica capsule; c) ball milled KNO<sub>3</sub>@silica capsule and d) particle size distribution of ground and ball milled sample*

### 2.3.2 FTIR analysis

Maintaining of chemical composition of ball milled  $\text{KNO}_3$  has been shown by FTIR analysis (Figure 9).

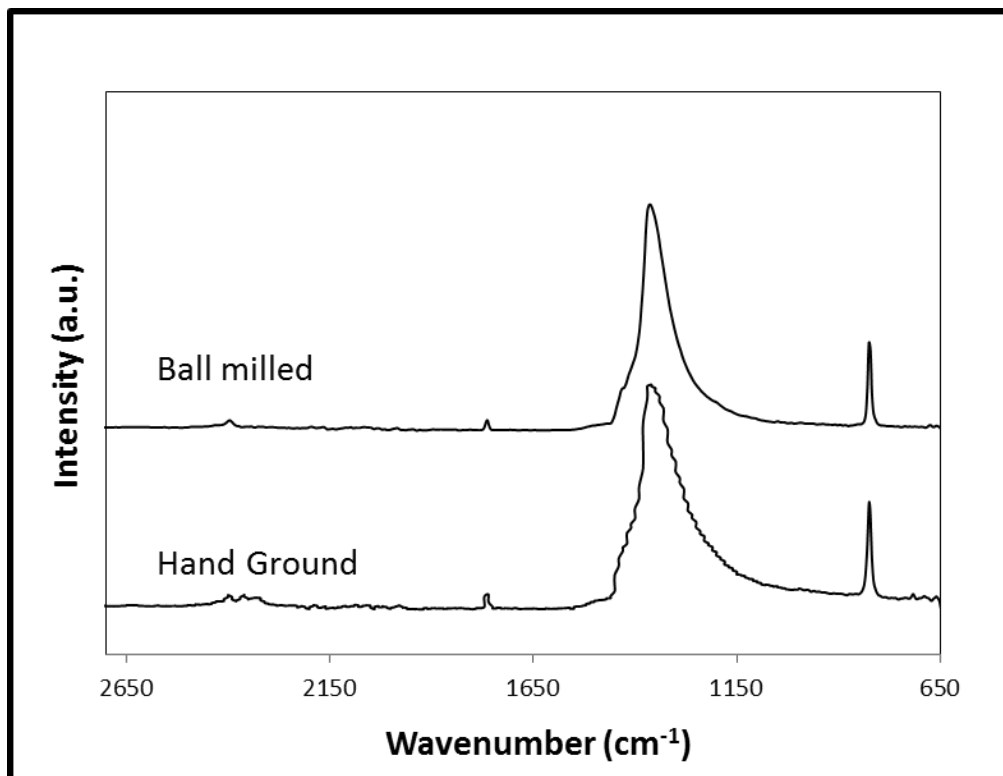


*Figure 9 FTIR comparison of hand ground  $\text{KNO}_3$  and ball milled  $\text{KNO}_3$*

### 2.3.3 Thermal analysis

DSC results shown in Figure 10a indicates S-BM1.5 has a lower onset of melting, which can be explained by the well-known size-dependent melting point depression.<sup>68, 69</sup> Same phenomenon is also observed for pure  $\text{KNO}_3$  salt samples with different size (Figure 10b).

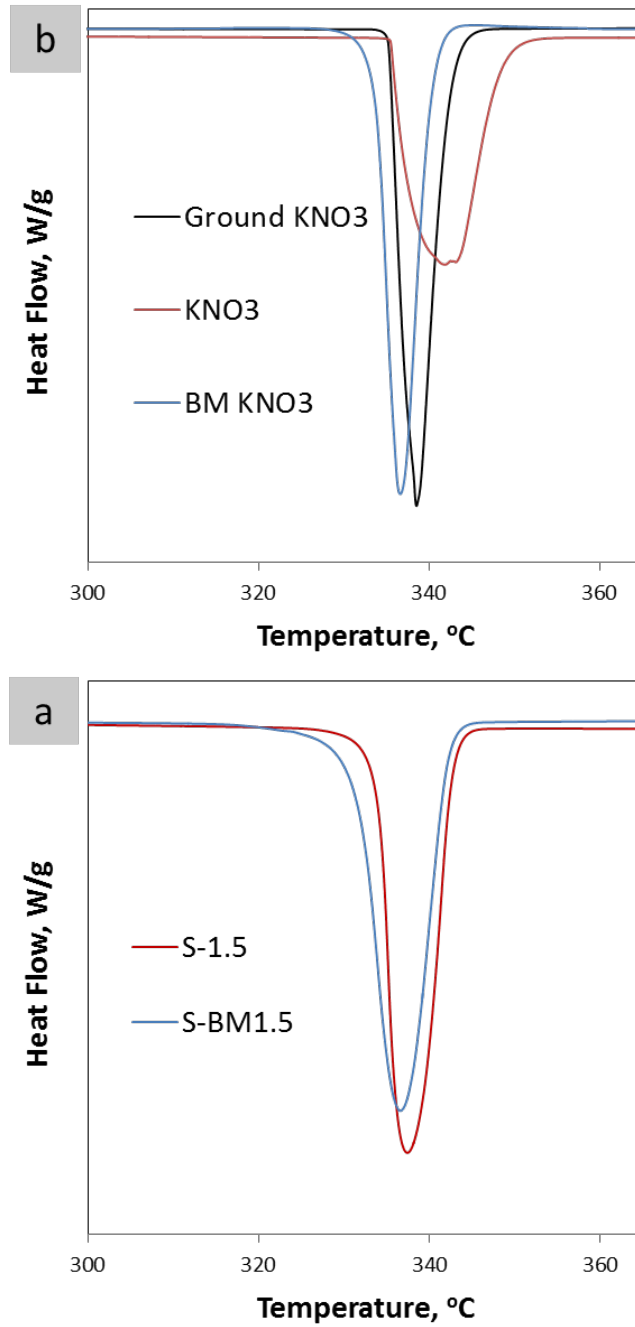


Figure 10 DSC analysis shows melting point depression and latent heat difference of a) 2<sup>nd</sup> cycle of S-1.5 and S-BM1.5; b) 2<sup>nd</sup> cycle of pure KNO<sub>3</sub> salt with different particle size

It is also observed that the latent heat of pure  $\text{KNO}_3$  varies with particle size, i.e. the latent heat of fusion for as purchased  $\text{KNO}_3$ , ground  $\text{KNO}_3$  and ball milled  $\text{KNO}_3$  are 103.1 J/g, 100.3 J/g and 98.0 J/g respectively. This size-dependent latent heat of fusion phenomenon has been reported by other researchers experimentally, as well as predicted by mathematical models.<sup>70-73</sup> Different models are provided to explain this phenomenon through a solid sphere core and the liquid surface theory,<sup>72</sup> where the latent heat of fusion is proposed as a function of the particle size and the liquid overlayer surrounding the solid particle.<sup>70</sup> On the other hand, the latent heat of the encapsulated sample with ball milling shows a significant improvement over ground sample (93.88 J/g vs 85.67 J/g). This indicates a higher encapsulation ratio for ball milled sample, which is hypothesized to be a result of lower TEOS condensation efficiency on the higher surface area of nuclei site (smaller particle of ball milled sample) in the dispersion.

#### 2.3.4 Effective heat capacity

Additives are reported to enhance the thermal storage performance of the high temperature HTF.<sup>74, 75</sup> With the latent heat of encapsulated PCMs, MEPCM are expected to give enhanced thermal storage performance.<sup>76</sup> Solar salt, a commercialized HTF for CSP, is used as the heat transfer media in this study.  $\text{KNO}_3$ @silica micro-encapsulations with different particle sizes were mixed with solar salt for the thermal analysis and rheological analysis. More specifically, S-G and S-BM were mixed with solar salt at different load (1%, 5%, 10% and 20%). The effective heat capacity of the MEPCM slurry was also calculated from the DSC testing result. MEPCM and solar salt powders were mixed in the Tzero hermetic pan and preheated at 200°C before transferring to DSC. 10 repeated heat and cooling cycles were then performed for the slurry. Excellent thermal

stability of the MEPCM in the slurry is demonstrated by the repeatable melting/solidifying peaks at the melting point of the MEPCM. Effective heat capacity of tested HTF was obtained by integrating the DSC specific heat data over the temperature range between 280°C to 400°C. With a latent heat of 11.2 J/g, 10w% MEPCM slurry improves the effective heat capacity by 11.0% over the pure solar salt, while the 5w% sample has a 9% improvement with a latent heat of 6.3 J/g. Although it is noticed that all samples have different specific heat capacity, illustrated by the different slopes of the curve at the non-phase change region in Figure 11a, more repeat tests need to be done to obtain accurate  $C_p$  values. The experimental uncertainty of specific heat of MEPCM slurry is from the non-uniform dispersion of the slurry. Molten salt nanofluid with enhanced specific heat was previously prepared in the literatures by a water based salt solution evaporation method.<sup>77,78</sup> Same method was found unsuitable for MEPCM slurry dispersion since the water soluble salt was not able to survive the vigorous water sonication process, illustrated by the TEM images of the hollow silica shell structure after sonication (Figure 4), where the shell thickness is approximated for S-1.5 and S-0.75 sample. An interesting comparison in Figure 11b shows the 10w% sample without sonication mixing (dot line) stores less thermal energy than the well mixed 10w% sample, due to the low  $C_p$ , eventually leads to a lower effective heat capacity than the base fluid at the given temperature range. For the 20w% sample, the disadvantage of low  $C_p$  when having larger portion of silica content in the sample is clearly shown in Figure 11a, despite the largest 24.6 J/g latent heat gain. Meanwhile, high  $C_p$  of 5w% is the main contributor of its effective heat capacity since its latent heat is the lowest among the samples.



As a proof of concept,  $\text{KNO}_3$ @silica microcapsules show the great potential of using high temperature MEPCM for HTF heat capacity improvement. Using the same encapsulation method for other molten salts with higher heat of fusion, effective heat capacity can be further improved.

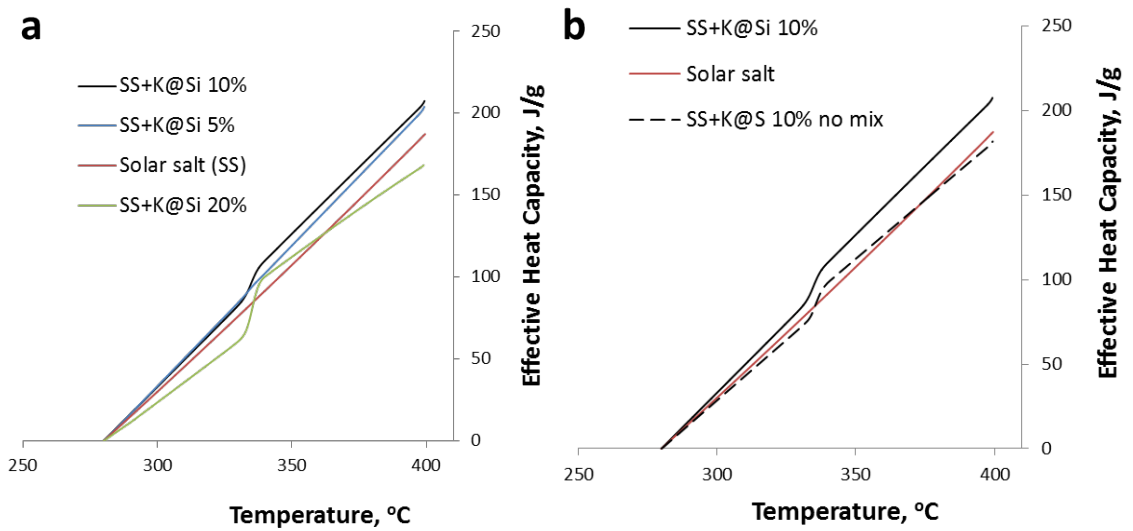
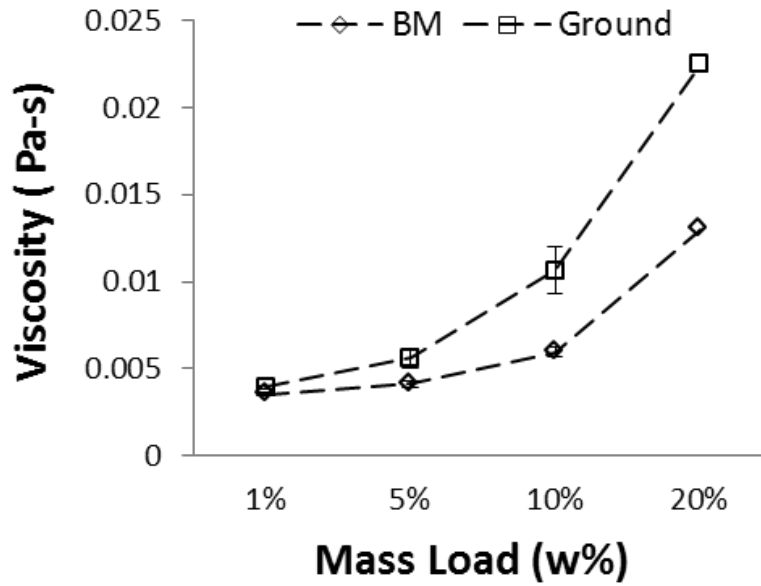


Figure 11 Effective heat capacity comparison among samples with different load

### 2.3.5 Rheological analysis

Viscosity is reported to increase with increasing load of micro/nano particle additives and is directly connected to pumping cost of the system which will be sacrificed to get better effective heat capacity.<sup>38, 79</sup> KNO<sub>3</sub>@silica micro-encapsulations with different particle sizes were mixed with solar salt for the thermal analysis and rheological analysis. More specifically, S-G and S-BM were mixed with solar salt at different load (1%, 5% and 10%), and then the viscosity of different mixture was obtained by using a rheometer. The viscosity was taken as the average of each sample at different temperature of 300°C, 350°C and 400°C. The values were observed constant for three repeated tests for the shear rate between 100 to 1000 s<sup>-1</sup>, indicate the MEPCM contained HTF behave as a Newtonian flow. The result is illustrated in Figure 12, where S-G 1w% and S-BM 1w% show clear different viscosity increment over pure HTF (14% and 3% respectively). Different particle size distribution is believed to be the reason behind the viscosity deviance.<sup>80</sup> This difference between S-G and S-BM is observed to be more significant at higher loading. The viscosity of S-G loaded HTF increases 64% and 210% compared to pure HTF for the load of 5 w% and 10 w% respectively, while the incremental values of S-BM loaded HTF are only 20% and 73%. It has been reported previously that the viscosity of the HTF will increase exponentially with the increased load of the micro particles as additive.<sup>81</sup> When connect to the pumping power, low viscosity of the smaller sized MEPCM is clearly a desired property for a cost effective system. The error bars in the plot shows the standard deviation of 3 repeated test of that particular sample. Since 20w% load was found to have a reduced effective heat capacity than base fluid and thus was not our interest, only one rheological test has been performed for each sample with a

result of 554% (ground) and 278% (BM) increased viscosity compare to base fluid respectively, just to illustrate the trend of viscosity increasing.



*Figure 12 Viscosity of HTF (solar salt) with different sized microcapsules as additive at a range of temperatures. Each viscosity value at a specific temperature is an average of measurements at shear rate from  $100\text{ s}^{-1}$  to  $400\text{ s}^{-1}$*

## **2.4 Conclusion**

This work is the first demonstration of using MEPCM slurry in high temperature heat transfer fluid to obtain enhanced thermal storage capability. Size of the MEPCM was studied to evaluate its impact on given HTF (molten solar salt). 11% enhanced heat capacity was observed comparing to the pure HTF with an excellent thermal stability been demonstrated. As a proof of the concept, the MEPCM slurry can be improved a lot in the future by obtaining well-mixed slurry, optimizing core-shell composition and using a molten salt with higher latent heat of fusion.

### 3. Chapter III – Thermal Performance Improvement: Binary Salt Microencapsulation

#### 3.1 Introduction

Micro encapsulated phase change materials (MEPCM) has been intensively studied as a latent heat storage (LHS) for thermal energy application.<sup>82, 83</sup> The capsule can prevent the leakage of PCM thus avoid the contamination of surroundings. Meanwhile, the micro-sized particles have better heat transfer rate and can be easily handled and integrated with various heat transfer media such like buildings and heat transfer fluid for different applications.<sup>35, 38-40, 52, 84-86</sup> However, most of the reported researches are for MEPCM working at low temperature ( $<300^{\circ}\text{C}$ ) which is only a small portion of thermal energy that can be harvested or recovered.<sup>10, 13, 52, 60, 63-65, 67</sup> PCM and the shell selection for high temperature MEPCM is quite limited since both of them need to have good thermal stability at elevated temperature. As a result, MEPCM working at high temperature is rarely available in literature. A  $\text{Sn}_x\text{Zn}_{1-x}$  alloy core silica shell MEPCM is reported to have a latent heat of 96 J/g at  $321^{\circ}\text{C}$ , however the effective heat capacity suffers because of the low specific heat of the alloy microcapsule ( $<0.4$  J/g-K). The MEPCM with the highest working temperature reported so far is an Al-25 wt% Si alloy core –  $\text{Al}_2\text{O}_3$  shell microcapsule at a phase change temperature of  $577^{\circ}\text{C}$  with a latent heat of fusion of over 247 J/g.<sup>5</sup> However this reported method has a heat treatment process to form boehmite coating which is solely applicable to the proposed alloy thus cannot be used for encapsulation of other materials. To the best of author's knowledge, abovementioned works are the only two reported examples of MEPCM operating at high temperature. Based on these research works, using PCM with higher specific heat and developing a

versatile encapsulation method can bring substantial improvement to high temperature MEPCM thermal storage.

Molten salts have much larger specific heat capacity than aforementioned metal and metal alloys (i.e.  $\text{Li}_2\text{CO}_3$  – 2.02 J/g-K at 327°C),<sup>87</sup> and their composites have wide range of melting point and latent heat that can be applied to different applications. For CSP application (290°C to 565°C), carbonate binary or ternary composition are decent candidates as they have a wide phase change temperature range from 397°C to 710°C with high latent heats of over 300 J/g.<sup>2</sup> In this work,  $\text{Li}_2\text{CO}_3$  (46.6) – 53.4  $\text{K}_2\text{CO}_3$  and  $\text{Li}_2\text{CO}_3$  (44.3) – 55.7  $\text{Na}_2\text{CO}_3$  binary salts were synthesized in-house as the core material for the high temperature MEPCM.

### **3.2 Experimental**

Binary carbonate salts were made in-house via evaporation of a mixed salt solution.<sup>78, 88</sup> Lithium carbonate (Sigma Aldrich) and potassium carbonate or sodium carbonate (Sigma Aldrich) were weighed precisely to the aforementioned composition and mixed before adding to a beaker of deionized water. The aqueous salt solution was sonicated in the bath sonicator for 1 hour to completely dissolve the salts. The mixed salt solution was then placed on a hot plate at 200°C until the solvent was completely evaporated. Remaining white binary salt sediment at bottom of the beaker was then heated up to 300°C to remove any intercalated water before scratched and collected from the beaker. The binary salt was then ground and transferred into a sealed vial and stored in a desiccator to avoid moisture absorption.

A ball mill was used to reduce the particle size of the as synthesized binary salt and to increase the uniformity of its particle size distribution. The powder after ball mill was heated again at 300°C to remove moisture. The binary salt micro particles were then dispersed in ethanol with polyvinylpyrrolidone (PVP) (Sigma Aldrich) for surface modification. PVP surfactant was readily loaded on binary salt particle surface after 24 hours stirring. The concentration of the salt (g) / surfactant (g) / solvent (ml) was kept as 1/1/40. After surfactant loading, the binary salt particles were washed and collected by centrifuge to remove unabsorbed PVP in the dispersion. The binary salt particles were then dispersed in an ethanol/ammonium hydroxide solution (Sigma Aldrich, 28%) mixture (1/0.04, v/v) with a probe sonicator. The sol solution is obtained by adding tetraethyl orthosilicate (TEOS) to above dispersion drop wise. The hydrolysis/condensation process of silica coating was let developed for 1 hour at 30°C under constant stirring. All the yield white microcapsules were then washed and collected by centrifuge.

To uniformly mix the microcapsules with HTF for the effective heat capacity test, as obtained binary carbonate salt@silica microcapsules were dispersed along with in-house synthesized binary nitrate salt (solar salt) powder together in ethanol by a bath sonicator with heating ability for 1 hour. Then the well mixed dispersion was allowed to evaporate while sonicating until the liquid level reached the bottom of the beaker. Then the dispersion was placed on a hot plate for the final drying. The resultant white powder mixture was collected from the beaker and ground in a mortar.

Field emission scanning electron microscopy (FESEM, Hitachi S-4800) and X-ray mapping was used to visualize the samples at different magnifications using an

accelerating voltage of 20 kV. Samples' chemical composition was characterized by Fourier transform infrared spectroscopy (FTIR, Thermo Nicolet 6700). Thermal analysis of all the samples was performed using differential scanning calorimetry (DSC Q20, TA Instruments).

### **3.3 Results and discussion**

#### **3.3.1 Lithium-potassium binary carbonate**

Lithium and potassium binary salt has been synthesized according to literature.<sup>78</sup> A sol-gel process was used for  $\text{Li}_2\text{CO}_3$  (46.6) – 53.4  $\text{K}_2\text{CO}_3$  binary salt @ silica (LiK@Si) encapsulation. The concentration of chemicals in the dispersion was kept at 1/1.5/20 (eutectic (g) / TEOS (ml) / ethanol (ml)). The FE-SEM images and x-ray mapping are provided in Figure 13 as a demonstration of encapsulation. Lithium was not detected in this case because of its low energy of characteristic radiation. Also, carbon signal can only barely be distinguished from the noisy background generated by the carbon tape used for SEM sample preparation. FTIR of original individual salts and the microcapsules are compared in Figure 14, which clearly illustrates that the LiK@Si microencapsulation shows both the  $\text{CO}_3^{2-}$  peaks from the salts and Si-O bonds from the silica.



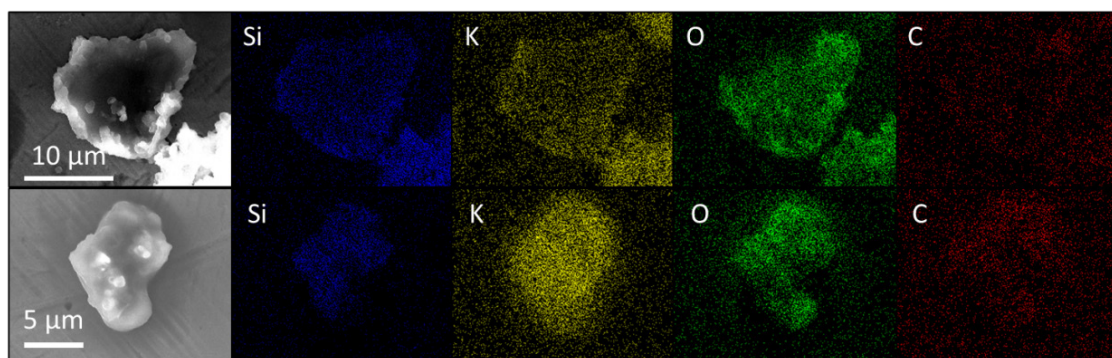


Figure 13 SEM imaging and x-ray mapping of LiK@Si capsule

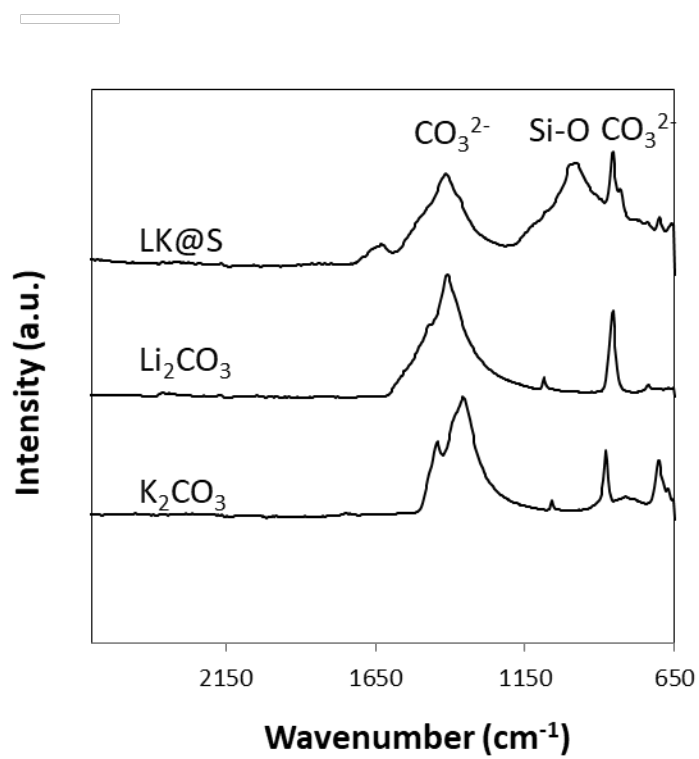


Figure 14 FTIR comparison of LiK@Si,  $\text{Li}_2\text{CO}_3$ ,  $\text{K}_2\text{CO}_3$

### 3.3.2 LiK@Si thermal analysis

Thermal analysis has been carried out using DSC. As synthesized  $\text{Li}_2\text{CO}_3\text{-K}_2\text{CO}_3$  salt has an on-set of melting at  $489.9^\circ\text{C}$  with a latent heat of  $326.2\text{ J/g}$ . This is considered close to the results from literature.<sup>2</sup> At the same time, a small double peak is observed at the 1<sup>st</sup> melting cycle, it is believed to be the result of incongruent melting of Li-K carbonate eutectic.<sup>89</sup> Also, it is noticed that the melting point decreased significantly to  $464.7^\circ\text{C}$  after 10 cycles with a reduced latent heat of  $264.5\text{ J/g}$  (blue dash line in Figure 15). This observation concurs with the work of Janz et. al. where the melting point of lithium and potassium binary carbonate reduced to  $460^\circ\text{C}$  to  $465^\circ\text{C}$  without  $\text{LiKCO}_3$  crystals in the system as seeds. It is hypothesized that there is a more stable crystalline phase for this specific binary salt at the lower temperature.<sup>89</sup> On the other hand, encapsulated salt (LiK@Si) shows lower latent heat ( $178\text{ J/g @ 1}^{\text{st}}$  cycle and  $126\text{ J/g @ 10}^{\text{th}}$  cycle) at the same melting point, shows typical encapsulation phenomenon as demonstrated previously.

Although the microencapsulation is successful, the inherited incongruent melting and phase separation of the  $\text{Li}_2\text{CO}_3\text{-K}_2\text{CO}_3$  eutectic make it undesirable for a constant charging / discharging thermal storage application. A binary salt with constant melting temperature and latent heat is needed instead.

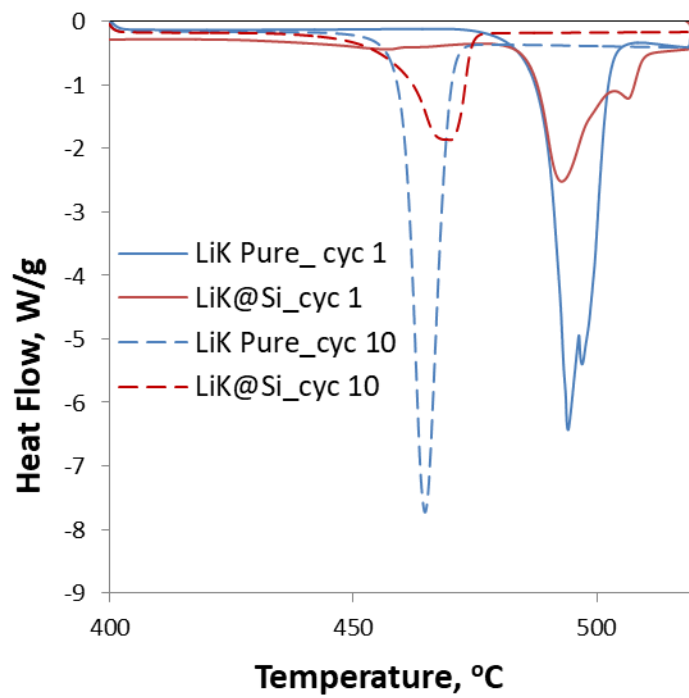


Figure 15 DSC comparison of LiK@Si binary salt

### 3.3.3 Lithium-Sodium binary carbonate

Unlike the lithium – potassium carbonate eutectic, lithium – sodium carbonate binary salt (LiNa) is considered as a simple eutectic that has congruent melting and no phase separation during phase change.<sup>89</sup> It also has large latent heat at a high temperature, i.e.  $\text{Li}_2\text{CO}_3$  (44.3) – 55.7  $\text{Na}_2\text{CO}_3$  melts at 498°C could give a latent heat of 393 J/g according to literature.<sup>2</sup>

Binary lithium and sodium carbonate salt was synthesized via above mentioned salt solution evaporation method. Then lithium-sodium binary carbonate salt encapsulated silica microparticles (LiNa@Si) were fabricated using the water limited sol-gel process.

FE-SEM images are provided to visualize the different surface morphology between the microcapsule (Figure 16a) and pure binary salt (Figure 16b), where the pure salt has a smooth surface under SEM while the microcapsule has a rough and bumpy surface, indicating the presence of silica shell. X-ray maps of key components have also been provided in Figure 16c and d to illustrate the distribution of silicon, sodium and oxygen, demonstrating their identical distribution as a core-shell structure. Lithium was not detected in this case because of its low energy of characteristic radiation. The particle size of the microcapsules is analyzed by ImageJ on several FE-SEM images similar to Figure 16e. The particle size distribution is illustrated in Figure 16f with an average particle size of 5.1(±2.1) nm.

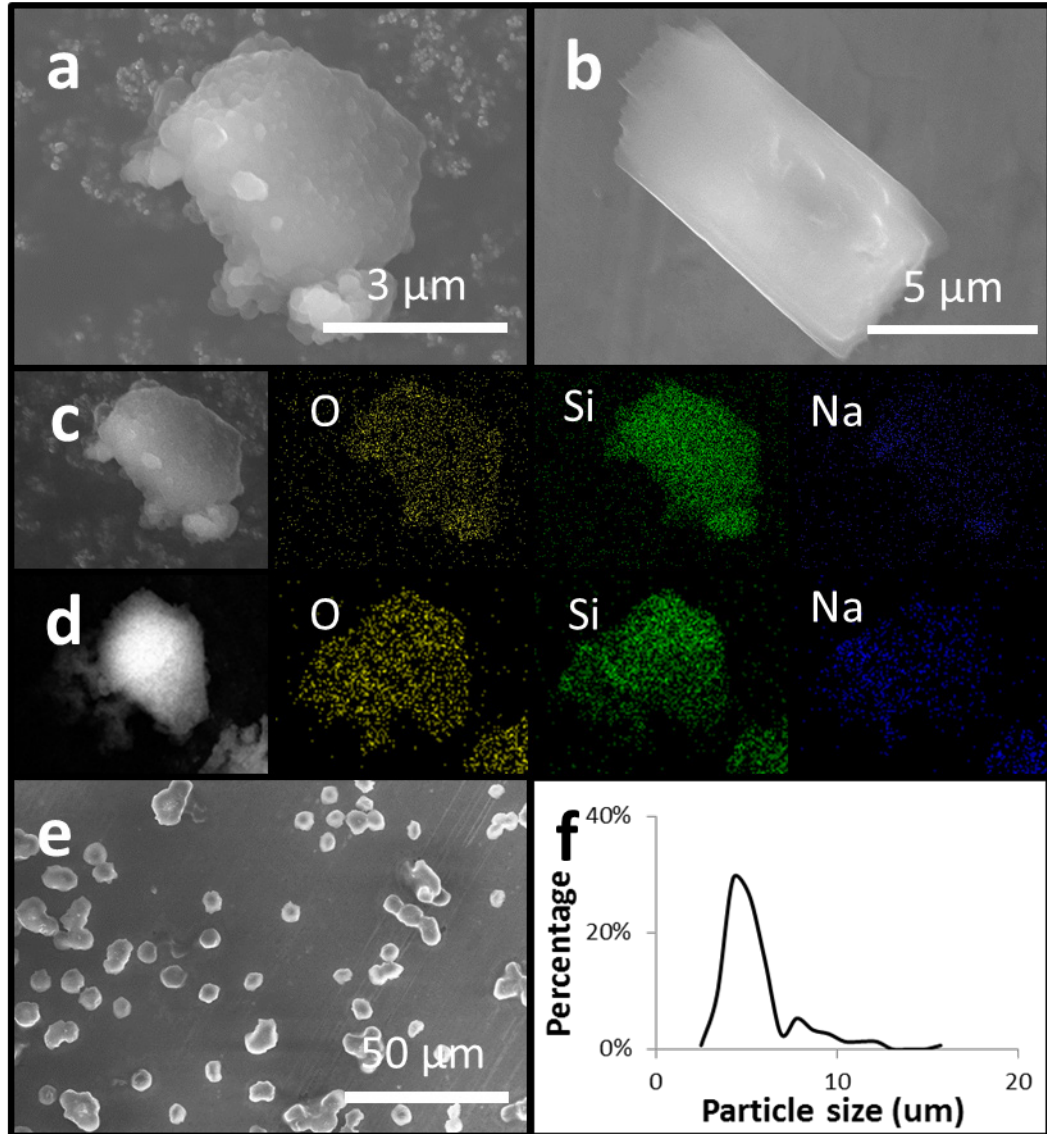
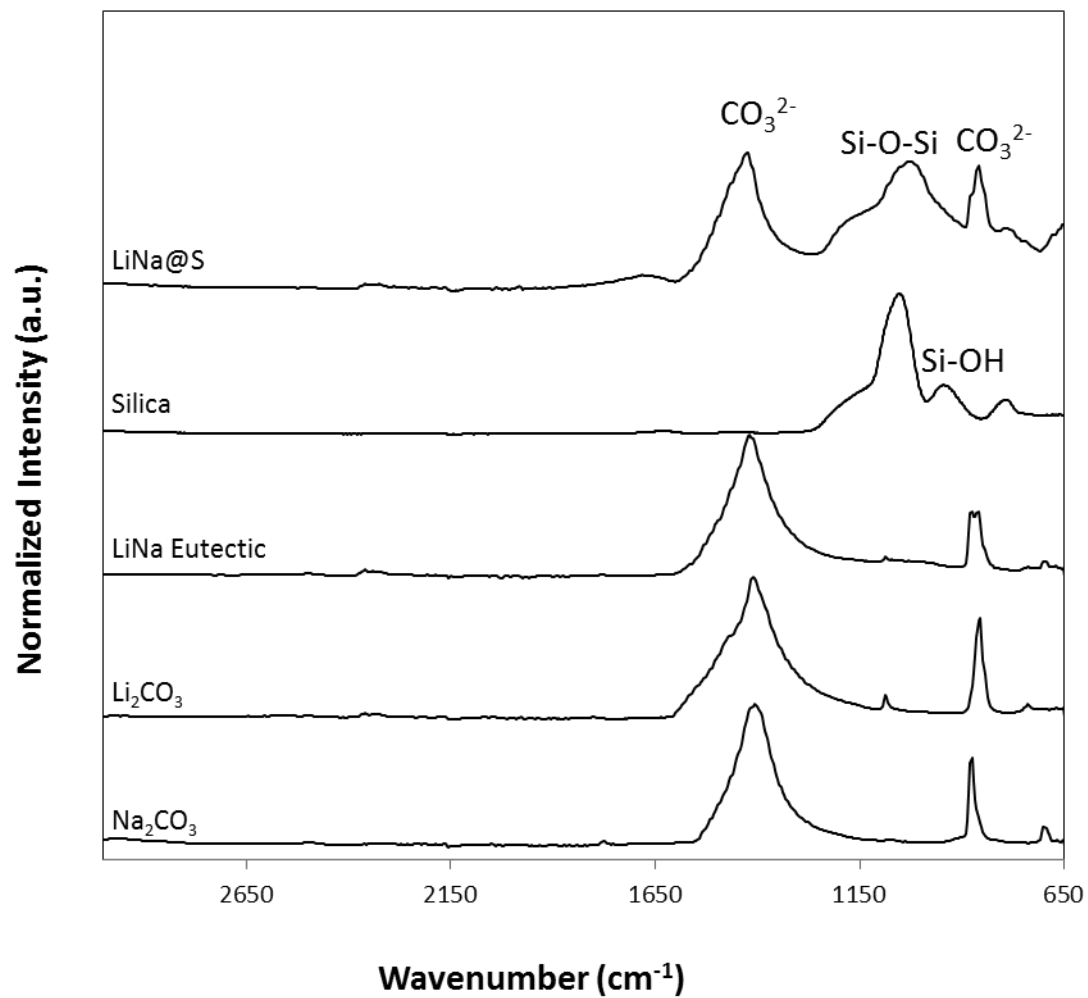


Figure 16 Morphology of a) LiNa@Si microcapsules and b) Pure LiNa eutectic; c) X-Ray map of LiNa@Si and e)&f) particle size distribution of LiNa@Si

Figure 17 shows the FTIR comparison of individual carbonate salt, the lithium-sodium binary salt and the LiNa@Si microcapsule. The peak around  $1410\text{ cm}^{-1}$  represents the typical  $\text{CO}_3^{2-}$  asymmetrical stretching band, while the peak at around  $876\text{ cm}^{-1}$  is the asymmetric  $\text{CO}_3^{2-}$  deformation band according to literatures.<sup>90, 91</sup> In the meantime, silica shows a large peak at  $1072\text{ cm}^{-1}$  and a small peak at  $957\text{ cm}^{-1}$ , represents Si-O-Si band and uncondensed Si-OH band respectively. At last, all the characteristic peaks from three different materials can be clearly located in the LiNa@Si microcapsule IR spectra, indicates the successful encapsulation and maintaining of individual chemical properties.



*Figure 17 FTIR comparison of individual carbonate salts, LiNa binary salt, silica and LiNa@Si microcapsule*

### 3.3.4 LiNa@Si thermal analysis

Lithium-sodium binary eutectic encapsulated silica nanoparticles (LiNa@Si) has been synthesized via previously mentioned water-limited sol gel silica coating process with different TEOS concentrations, i.e. the concentrations of binary salt/TEOS/Ethanol (g/ml/ml) were kept at 1/1.5/20 and 1/2/20, and they will be named as LiNa@Si-1.5 and LiNa@Si-2 respectively in following context. Differential scanning calorimetry (DSC) was used for thermal performance analysis from 400°C to 540°C at a temperature ramping rate of 3°C/min, however, solidification characteristics of the sample was not regarded as the study subject of this work since the cooling rate was not controlled by the instrument. Similar amount of sample was load into Tzero hermetic pan for each test in order to keep the consistency. All loaded pans were preheated on a hot plate for 30 mins at 200°C prior to the DSC test.

Phase change characteristics of microcapsules and pure eutectic sat are shown in Figure 18. The pure binary salt has an onset of melting of 498.6 °C which identically matches the melting point reported in literature. The slightly lower latent heat of fusion (360.5 J/g) compared to the literature (393 J/g) could be resulted from the composition mismatch caused by non-uniformity of the mixing during the binary salt synthesis. LiNa@Si-1.5 exhibits a latent heat of 250.9 J/g at an onset of melting of 498.6, which leads to the encapsulation ratio of 69.6%. On the other hand, LiNa@Si-2 is only able to recover a latent heat of 131.3 J/g because of the much higher silica content in the encapsulation.



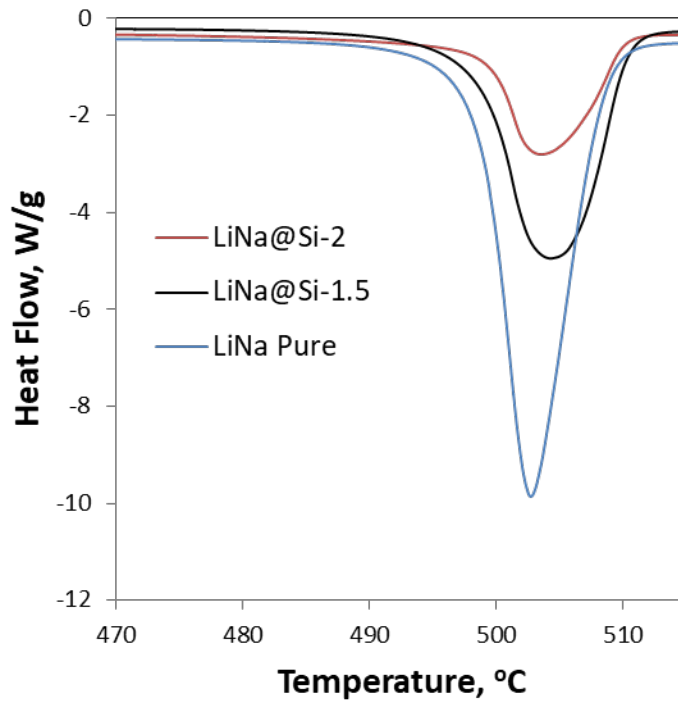


*Figure 18 Latent heat of fusion for LiNa@Si-1.5, LiNa@Si-2 and the pure eutectic*

Compared to the encapsulation ratio of the single salt encapsulation, i.e. over 80% for the  $\text{KNO}_3@silica$  microcapsules, the lower encapsulation ratio achieved on  $\text{LiNa}@Si$  is not fully understood, it is likely salt composite structure has been partially changed during the long surfactant loading and silica coating process due to the different solubility of the individual salts in ethanol.

The salt composite microcapsules are found thermally stable over 10 cycles. In Figure 19, different cycles of the thermal test of pure salt composite and the microcapsules are compared to demonstrate the thermal reliability. Sodium carbonate is reported to have a higher vapor pressure than potassium carbonate and is considered easier to decompose.<sup>92</sup> The effect of heating rate is also found directly affecting salt decomposition.<sup>93</sup> In order to mitigate the decomposition of the salt, a lower temperature ramping rate ( $3^\circ\text{C min}^{-1}$ ) was used for all the carbonate salt tests. Pure salt composite has a slight on-set of melting shift to  $498.3^\circ\text{C}$  after 10 cycles, however, it can still recover most of the latent heat ( $358.7\text{ J/g}$ ), indicates a good thermal reliability of the pure carbonate salt composite. In contrast, a noticeable latent heat drop from  $250.9\text{ J/g}$  to  $215.9\text{ J/g}$  of  $\text{LiNa}@Si-1.5$  sample is observed from 2<sup>nd</sup> to 3<sup>rd</sup> heating cycle. This is suspected to be a result of disordered binary salt structure after the long surfactant loading and silica coating process. Interestingly, the melting of the microcapsule is more consistent after the 3<sup>rd</sup> and a latent heat recovery of  $220.7\text{ J/g}$  is observed at the 10<sup>th</sup> cycle, indicating  $\text{LiNa}@Si-1.5$  sample becomes more stable after the initial cycling. The latent heat values of 10 cycles are illustrated in Figure 20.

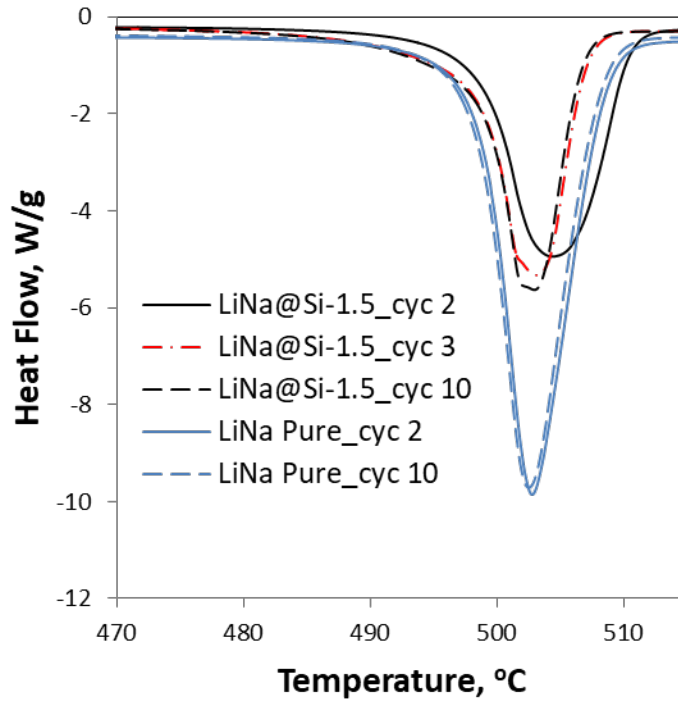


Figure 19 Thermal reliability of LiNa@Si-1.5 and pure salt composite over 10 cycles

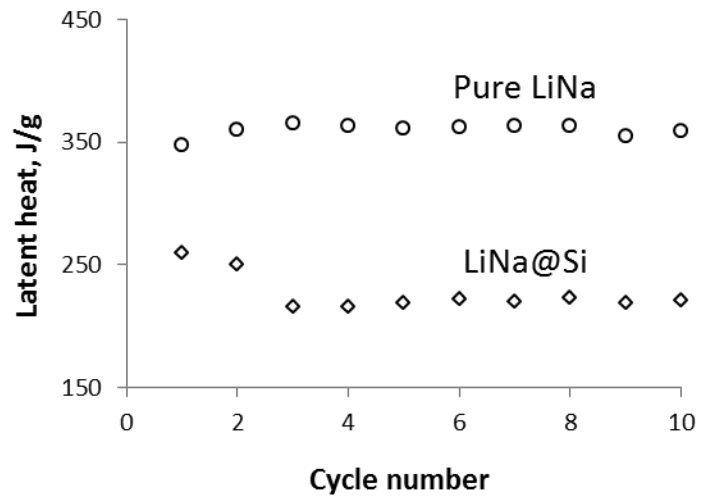
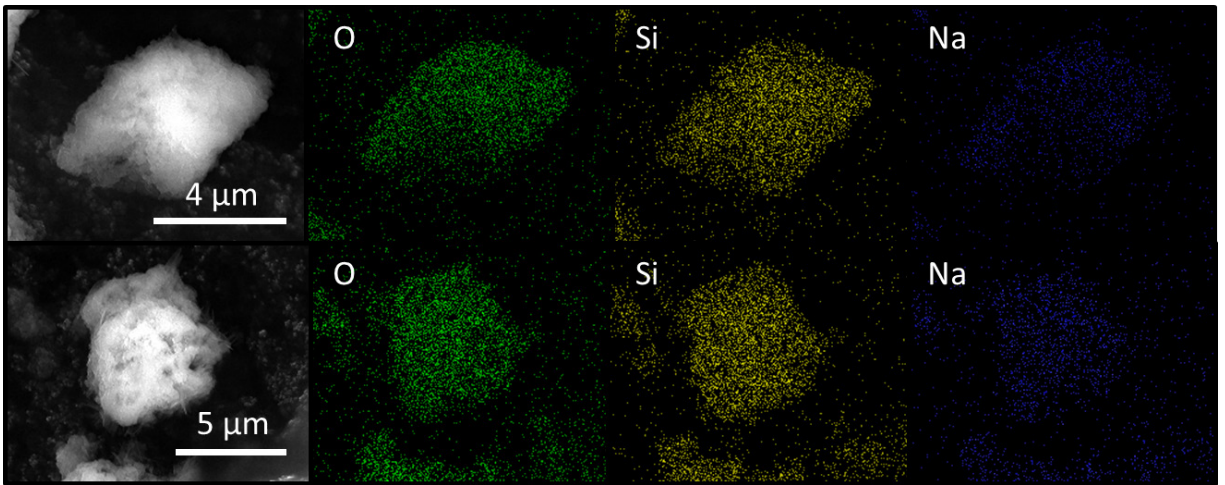


Figure 20 Latent heat values of 10 cycles for LiNa@Si-1.5 and Pure LiNa salt

### 3.3.5 Thermal stability of LiNa@Si after DSC

LiNa@Si microcapsules after 10 DSC test cycles were removed from the Tzero hermetic pan for thermal stability characterization. The retention of its powder form after test indicates no salt leakage happened during the thermal cycling. In contrast, exposed salt will tend to form a continuous film covering the bottom and wall of the pan. Appendix 7 shows the photos of both scenarios.

The powder after DSC test was then directly pressed on the carbon tape without any washing for FE-SEM examination. In Figure 21, x-ray mapping shows intact core-shell structure is maintained perfectly after thermal cycling. However, it is also noticed that the morphology of silica shell does look rougher than as prepared sample.



*Figure 21 X-ray maps of LiNa@Si-1.5 sample after 10-cycle DSC test*

FTIR was then utilized to investigate the chemical composition of the microcapsule after thermal cycling. To avoid moisture absorption, FTIR test was done immediately after DSC test. IR spectra of LiNa@Si-1.5 sample before and after thermal cycling at 540°C are shown in Figure 22. An additional peak around 960  $\text{cm}^{-1}$  is clearly observed after thermal cycling, represents the Si-OH band formed via the oxidation of uncondensed ethyl group in air at high temperature. This phenomenon is also reported in literature where alkyl group gets converted to Si-OH after silica had been calcined at temperature higher than 420°C. At a high enough temperature, dehydration will happen to transform Si-OH group to siloxane bridge (Si-O-Si).<sup>94</sup> Interestingly, another additional peak at 736  $\text{cm}^{-1}$  is also observed after thermal cycling, which represents the N-H wagging.<sup>95, 96</sup> According to literature, PVP readily decomposes to monomers at temperature of 490°C.<sup>97</sup> It is likely that the vinyl pyrrolidone after PVP decomposition is the contributor to the additional peak. More investigation is needed to fully understand the change of the shell's chemical composition, however the study is beyond the scope of this work and will be continued in future work. Most importantly, from above mentioned thermal stability test results, although it is noticed that structure of silica shell of the microcapsule tends to be changed by high temperature calcination, it is still strong enough to with stand the thermal treatment at 540°C. This stabilizing period is believed to be one of the reasons causing the inconsistent thermal performance of the microcapsule. In order to fully understand the thermal stability of the microcapsule, longer test cycles need to be performed.

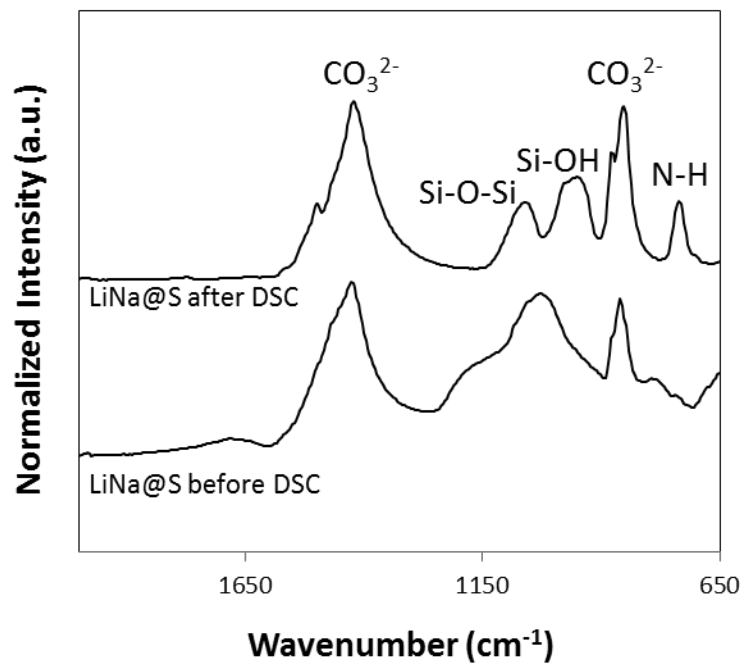


Figure 22 FTIR spectra of LiNa@Si-1.5 before and after 10-cycle DSC test



### 3.3.6 Effective heat capacity – active configuration

High temperature MEPCM can be found useful in lots of applications, among which concentrating solar power (CSP) plant is the one with the harshest environment. Most of the MEPCM are not compatible with the high temperature and highly corrosive HTF (molten salt). Successful incorporation between molten salt and silica has been reported previously in literature,<sup>98</sup> making LiNa@Si microcapsule a promising MEPCM to be used with molten salt HTF for heat capacity enhancement.

Most of the CSP with solar tower technology use active 2-tank direct configuration where solar salt acts as both thermal storage media and HTF and is circulating between a cold tank and a hot tank at temperature of 292°C and 565°C respectively.<sup>99, 100</sup> This configuration requires the HTF to store solar thermal energy, as much as possible, within designed temperature range. More importantly, the cold tank temperature needs to be kept above the solidification temperature of solar salt (220°C) during the night hours to avoid clogging in the circulation. In this work, the effective heat capacity of solar salt (SS) with as prepared MEPCM as additive is calculated from DSC heat flow data and compared for different MEPCM loading percentage.

In order to achieve a well-mixed sample, LiNa@Si-1.5 microcapsules and SS powder were dispersed with ethanol in a beaker then sonicated in a heated bath sonicator. The solvent was allowed to evaporate until the liquid level reached the bottom of the beaker, after which the rest of dispersion was left on a hot plate at 200°C until completely dry. The powder was collected from the bottom of the beaker and preheated at 200°C before the test.

The effective heat capacity results are compared among different MEPCM sample load of 0% (pure SS), 5%, 10% and 20% for the temperature range from 400°C to 540°C. In Figure 23, it is obvious that loading is the dominant factor of the effective heat capacity, with the highest enhancement of 40.5% observed for 20% load. The high specific heat capacity of lithium-sodium carbonate composite, visualized from the initial slope of the integration, is clearly one of the reasons for this enhancement. Nevertheless, no clear ‘jump’ (representing latent heat) is observed from the integration, implying the melting of the MEPCM is in a large temperature range. This observation is supported by the heat flow curves from DSC data (Appendix 8), where no clearly defined melting peak is observed for the LiNa@Si and SS mixture over 10 cycles. This rather complex melting behavior is hypothesized to be a result of solar salt decomposition at high temperature. The decomposition of solar salt at high temperature is confirmed by DSC thermal cycling (Appendix 9) as well as the literature, where NO and NO<sub>2</sub> gas was readily detected at the temperature over 400°C.<sup>101</sup>

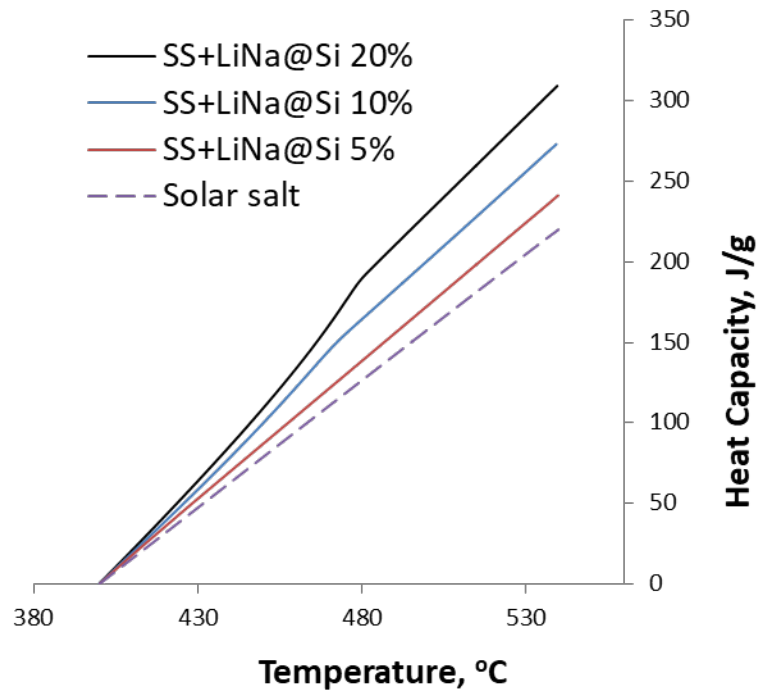


Figure 23 Effective heat capacity results of LiNa@Si and SS mixture at different load

### 3.3.7 Effective heat capacity: passive 2-tank indirect storage scenario

As the most mature concentrating solar power technology, the 2-tank configuration uses solar salt as the thermal storage media in order to have a forced active heat transfer. As a result, the storage performance is restricted to the effective heat capacity of solar salt. Moreover, currently auxiliary heat has to be supplied to keep the HTF above the freeze point. An indirect design is to separate the function of thermal storage and heat transportation. In this case the heat can be stored in the thermal storage material so that another HTF fluid with lower freezing point can be used in the circulating system. The drawback is the expensive heat exchanger. Currently most of the parabolic through plants use the 2-tank indirect design operating with the solar salt.

Unlike the active molten salt thermal storage, passive thermal storage media do not circulate in the system. It is possible that by replacing the molten solar salt in the 2-tank thermal storage system with molten salt microcapsules will improve the effective heat capacity, reduce the auxiliary heat during the night, and avoid corrosion to the tank. Furthermore, two MEPCM with different phase change temperature can be used for hot and cold tank to further optimize the heat capacity and increase the Rankine cycle efficiency.

Additionally, the possibility of using PCM as solid thermal storage material directly in passive and thermocline storage system has already been studied.<sup>102, 103</sup> The drawback of passive storage system, compared to active direct system, is the excessive cost to build heat exchanger and possibly lower heat transfer rate. As a demonstration of concept,

LiNa@Si-1.5 and solar salt is compared in Figure 24 to demonstrate the enhancement for hot tank, meanwhile  $\text{KNO}_3$ @silica is used for the cold tank (Figure 25).

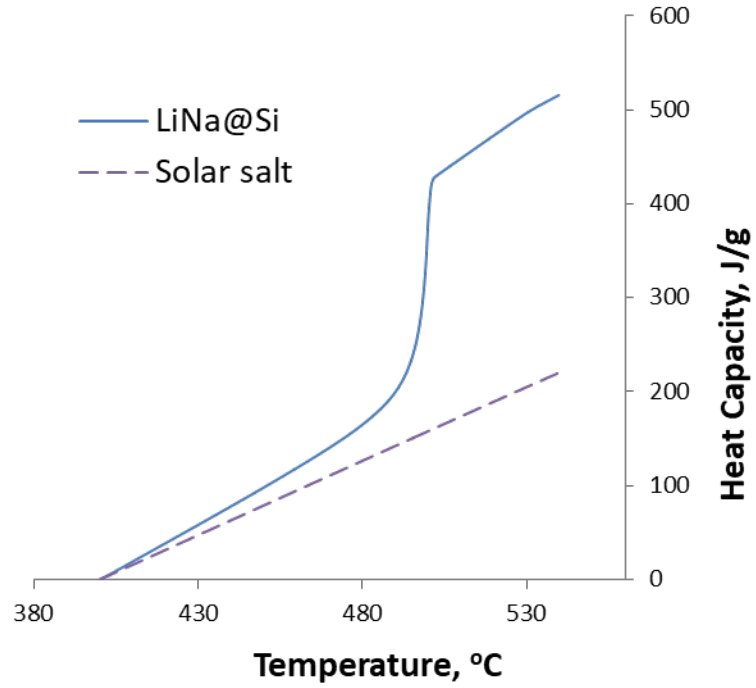


*Figure 24 Effective heat capacity of LiNa@Si for a passive hot tank storage*

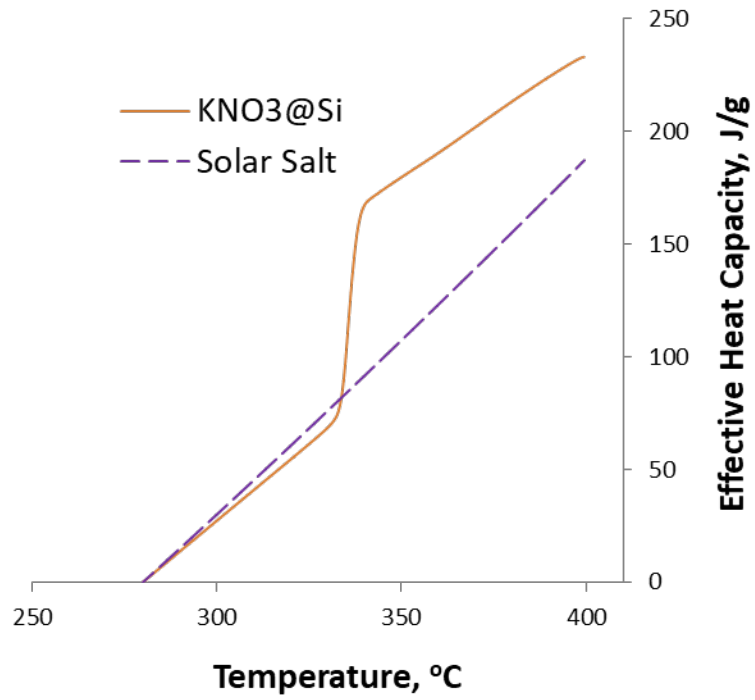
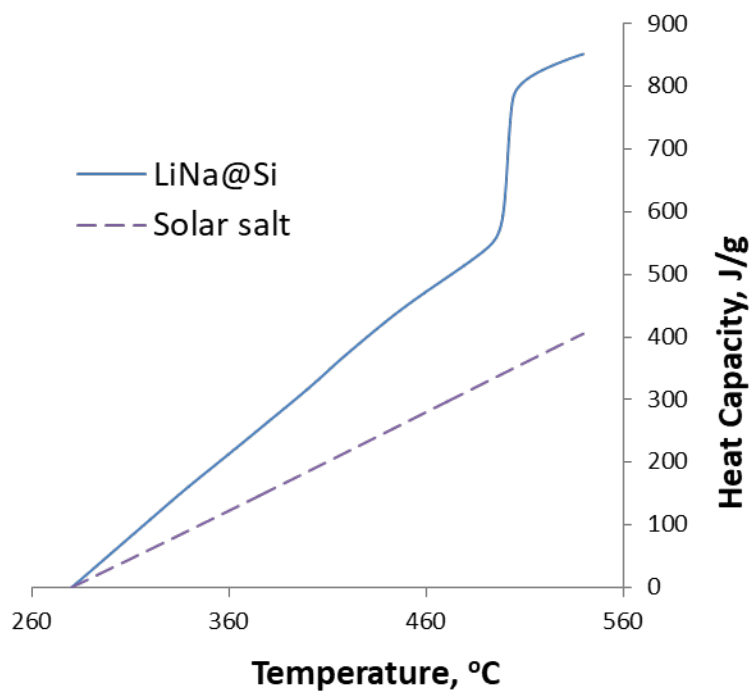


Figure 25 Effective heat capacity of K@S for a passive cold tank storage

In Figure 24, an enhancement of 134.4% on effective heat capacity is obtained from the temperature range of 400°C to 540°C for LiNa@Si-1.5 over solar salt. This remarkable improvement can be attributed to the high specific heat capacity of the MEPCM as well as the extra latent heat of fusion from binary carbonate salt. The additional thermal energy stored can be used to power the system during the time with insufficient solar energy supply. In Figure 25, despite of the lower specific heat, KNO<sub>3</sub>@silica microcapsule still outperformed solar salt on the effective heat capacity by 24.6% between the temperatures of 280°C to 400°C. This extra energy stored can be used to warm the HTF during the night hours.

For 1-tank passive storage configuration, concrete and solar salt are used as the thermal storage media.<sup>98, 102</sup> To compare the thermal performance between LiNa@Si-1.5 and solar salt, the effective heat capacity of both materials is calculated from the temperature range of 280°C to 540°C. An enhancement of 110.1% is observed for binary carbonate microcapsules. This extra heat can be used for the overall thermal cycle. Besides, the MEPCM can decrease the risk of contamination and corrosion which has been a problem for using pure solar salt as thermal storage media.

In summary, as a passive thermal storage media, binary carbonate salt microcapsule exhibits tremendous effective heat capacity enhancement over current best product. This MEPCM is also believed to be universally applicable to any other high temperature thermal storage applications.



*Figure 26 Effective heat capacity comparison of LiNa@Si-1.5 and SS for passive 1-tank storage*



### **3.4 Conclusion**

High temperature compatible binary carbonate microcapsule has been successfully synthesized first time. The microcapsules are thermally stable for 10 cycles with a latent heat of over 220 J/g at 498°C. As a proof of concept, the as synthesized LiNa@Si microcapsules are investigated in CSP plant application with two different design concepts. The MEPCM demonstrates enhanced effective heat capacity of 40.5% and 134.4% over best commercialized product for active and passive solar thermal systems respectively. The reported MEPCM is also compatible with other thermal energy storage applications at high temperature.

#### **4. Chapter IV: Versatility of the encapsulation method**

As a versatile encapsulation method, proposed silica coating technology can be used for encapsulation of different materials, different particle size and different core-shell structure. This chapter is to demonstrate the versatility of the encapsulation method by showing the silica encapsulation of different materials at different particle size.

##### **4.1 Stainless steel nanocapsules**

Next generation thermal storage requires the material that operates above 1000°C. There is no micro or nano-encapsulation of PCM reported working at this high temperature. To pushing the boundary, stainless steel (MP 1400~1450°C) encapsulated silica nanoparticles is demonstrated, which can be the first step toward next-gen thermal storage.

Stainless steel 304 nanoparticles are encapsulated in silica to demonstrate the capability of metal encapsulation. FE-SEM images and x-ray mapping are provided in Figure 27 to show the preliminary result of encapsulation. Clear core-shell structure can be seen under SEM at accelerating voltage of 20kV. It is shown in Figure 27a that there is excessive silica nanoparticles formed during the encapsulation process, results from insufficient surface area for TEOS to condense on. This problem can be solved by increasing steel nanoparticle concentration, decreasing TEOS concentration and increasing the stability of steel nanoparticle dispersion.

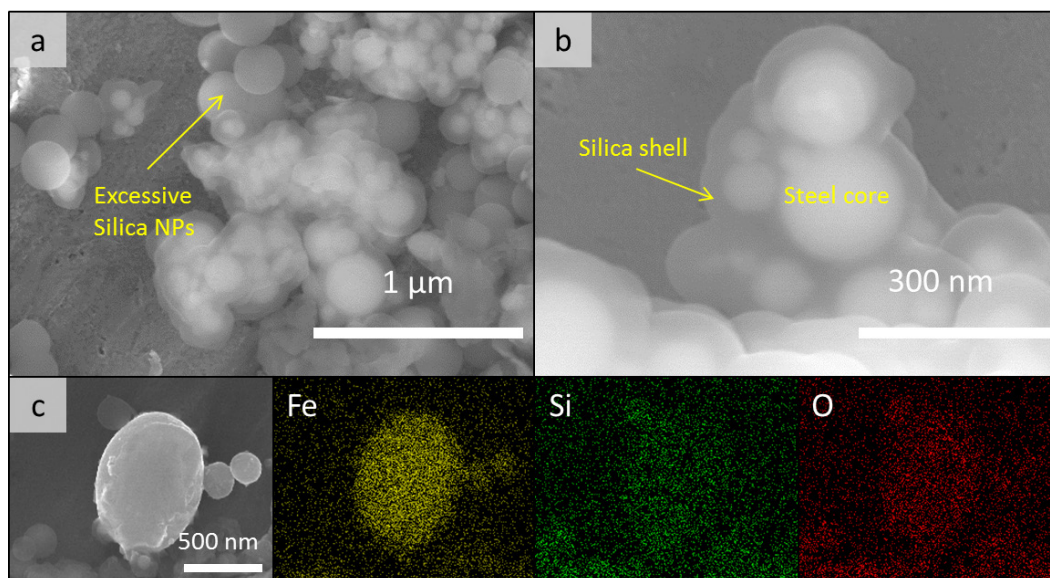


*Figure 27 SEM image and X-ray mapping of stainless steel encapsulated silica nanoparticles*

## 4.2 Gallium microencapsulation

As a low melting point metal, gallium can find a lot of applications at moderate temperatures. Figure 28 shows the FE-SEM images of gallium@silica encapsulation. This interesting image shows the ruptured shell during gallium expansion under electron beam. This is an indication that for some materials with high volume expansion during phase change, a void between the core and shell may be needed.

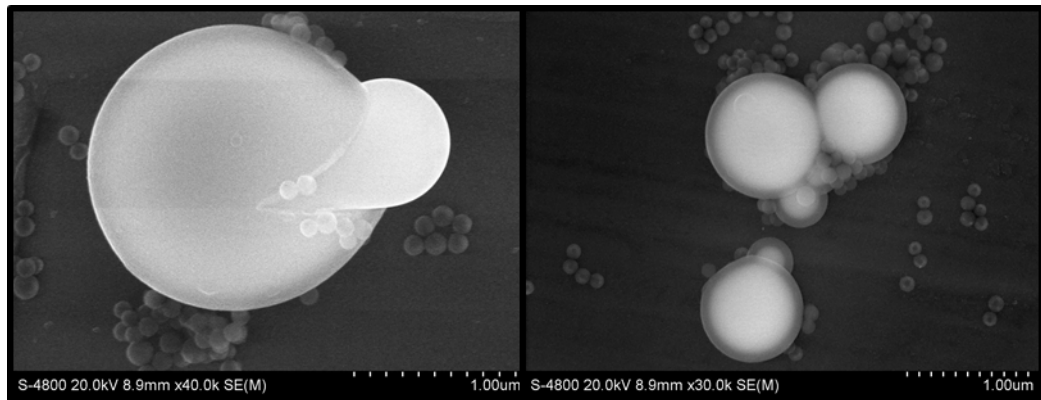


*Figure 28 Gallium@silica microencapsulation*

### 4.3 Hollow silica shell and void creation

Hollow silica nanoparticle is the first step of creating void for the core-shell nanostructure. Below is a demonstration of fabrication of hollow silica nanoparticles with characterization of its chemical property and porosity.

#### 4.3.1 Formation of core-shell silica

The synthesis of hollow mesoporous silica particles is identical to the fabrication process reported by Shi et al.<sup>14</sup> Conventional Stöber method was used for silica formation. 10 ml water and 1.3 ml ammonium hydroxide solution were added to 71 ml ethanol. After 10 minutes bath sonication, this base solution was heated up to 30°C on a hot plate, 3 ml tetraethyl orthosilicate (TEOS) was then added into the solution and kept at 30°C for 1 hour under a vigorous stirring to allow the sol-gel process to complete. During this hydrolysis and condensation process, the original transparent solution changed to a whitish dispersion with visible particles indicating the formation of Stöber silica nanoparticles. At this point, a solution mixed by 2 ml TEOS, 0.8 ml octadecyltrimethoxysilane (C<sub>18</sub>TMS) and 16.5 ml ethanol were injected into the dispersion dropwise by a syringe pump at a speed of 4 ml/hour, the dispersion was also kept at 30°C with stirring during the injection. After this, the dispersion was kept at the same temperature and stirring condition for another hour to form the mesoporous shell on the solid silica nanoparticle.

#### 4.3.2 Fabrication of hollow silica nanoparticle

To obtain the hollow mesoporous silica nanoparticles, as prepared core-shell silica was etched in 0.1 M Sodium carbonate solution at 80°C for 20 minutes under vigorous stirring. As reported by Shi et al.<sup>16</sup>, the different condensation degree between mesoporous silica shell and solid silica core enables the selective etching of the core-shell structure. The less condensed solid silica gets etched away faster than mesoporous silica which has a higher condensation degree. Obtained hollow silica particles were carefully washed by a centrifuge couple of times using water and ethanol consecutively. The sample was then kept in a centrifuge tube with ethanol for at least 24 hours to let ethanol to completely replace the original liquid (mostly water) in the hollow particles, with the intention of avoiding shell collapsing during drying caused by capillary stress. Drying was done at 50°C in an oven for 24 hours at atmosphere pressure.

#### 4.3.3 Morphology of hollow silica nanoparticle

Etching of the core is crucial to the synthesis of hollow porous silica nanoparticles. Shi et al. has claimed that the selective etching of silica is achieved because of the different condensation degrees between the core (solid silica) and shell (mesoporous silica).<sup>16</sup> For the etching to be thorough and uniform, both etchant concentration and core-shell silica particle concentration need to be controlled. Meanwhile the silica needs to be dispersed well in the dispersion. Shi and co-workers reported different etching results for various etchant concentrations. However, the effect of the concentration of core-shell silica particles in the dispersion is unneglectable as over-etching or incomplete-etching can happen for inappropriate core-shell silica concentrations, which has been shown in

Figure 29b, c and d. Complete etching was observed when the concentration of core-shell silica particles was kept at 2 mg/ml (Figure 29c), while incomplete-etching was observed when the core-shell silica concentration is higher, for instance, in Figure 29b, leftover of core material can be seen from TEM image when the silica concentration was set at 5.7 mg/ml. In this case, further increasing of the etchant concentration would not help as severe coagulation of silica particles was observed possibly because of the changing of ion concentration in the solution leads to the alteration of surface charge on the nanoparticles. On the other hand, over-etching happens when the concentration of silica is too low in the dispersion. As shown in Figure 29d, the selective etching effect was not observed and the whole structure was destroyed and fused together when the concentration of silica was 1.3 mg/ml. The etchant concentration of all the experiments above was maintained at 0.1M (sodium carbonate in water).

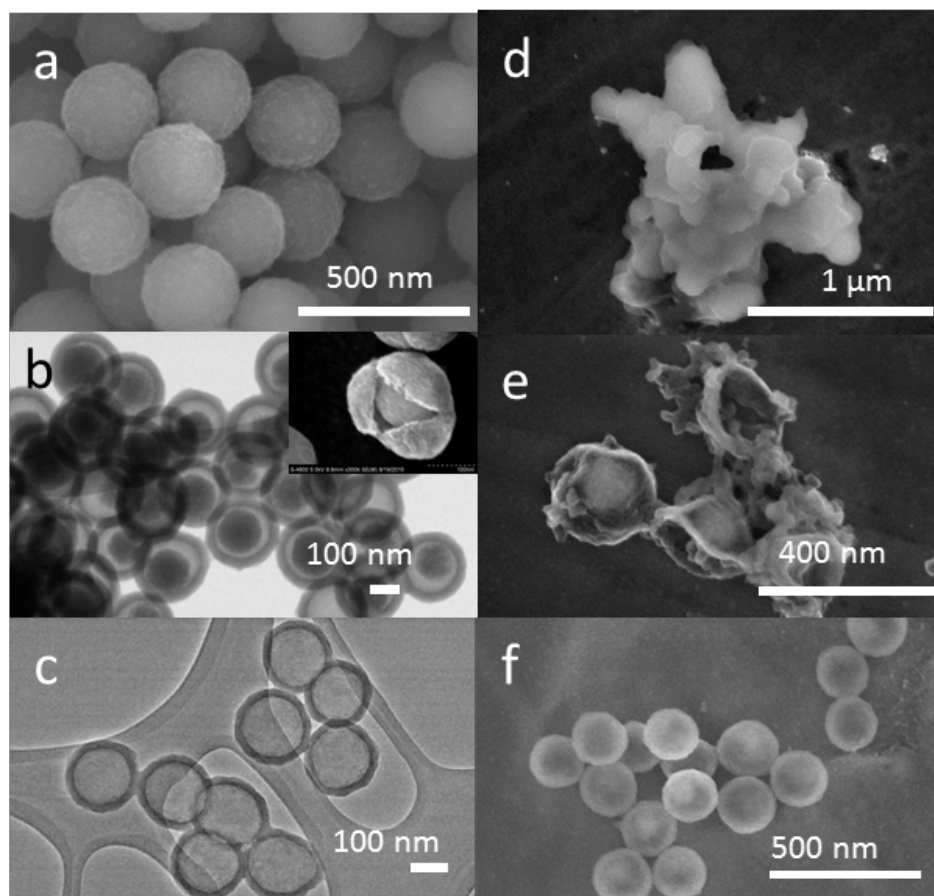


*Figure 29 SEM and TEM image of hollow silica nanoparticles*



It is also noticed that there is a slight decreasing in average particle size after etching. For example, the particles size of as prepared core-shell silica is measured from SEM image as  $295(\pm 13)$  nm by ImageJ, while the particles size of etched silica decrease to  $238(\pm 12)$  nm.

Drying process is another crucial step to get the final product. Those delicate silica and polymer structures can be dramatically changed under different drying conditions.<sup>104-106</sup> Capillary stress induced by water evaporation during drying was found to have a negative impact on the hollow structure in the way of causing shell collapsing and breaking. Typically, this shell collapsing effect can be mitigated by increasing the shell thickness, using an alternative liquid with low surface tension or controlling the drying condition such like via freeze or supercritical drying. In this case, ethanol was used, because of its low surface tension, to substitute the water based solution left in the hollow particles after etching. The visual comparison of dried particle after etching between water dry and ethanol dry is shown in Figure 29e and f respectively. Almost all the particles collapsed for water dried sample while none collapsed shell was found for ethanol dried.

Condensation degree of solid silica core and mesoporous silica shell is compared by Fourier transform infrared spectroscopy (FTIR). Figure 30 clearly shows that solid silica core has more Si-OH bonds than mesoporous silica shell by comparing the relative peak intensity at  $953\text{ cm}^{-1}$ . The Si-O-Si bond of mesoporous silica shell shows a red shift from  $1060$  to  $1064\text{ cm}^{-1}$  compare to that of solid silica core, indicating a more open structure on the shell. When comparing to Shi's work, the peaks of the obtained sample have a red shift for both mesoporous silica and solid silica.<sup>15, 107, 108</sup>

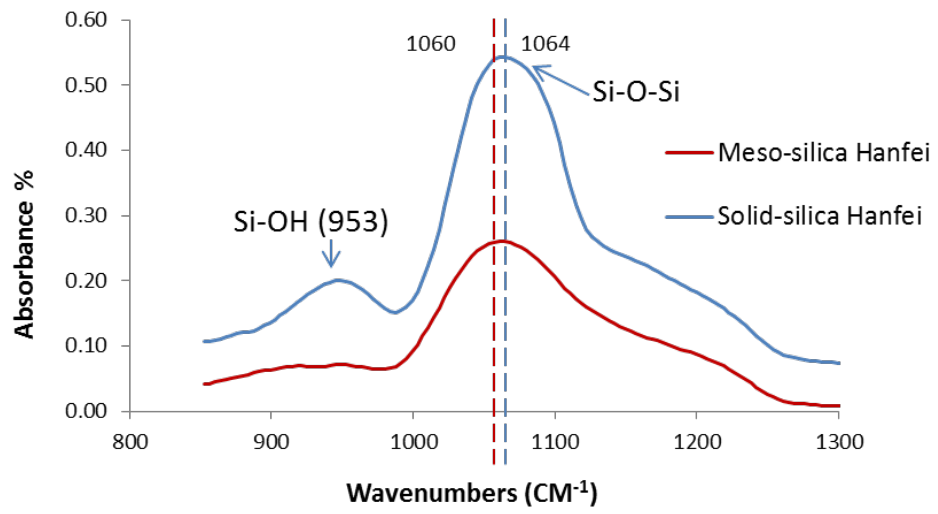
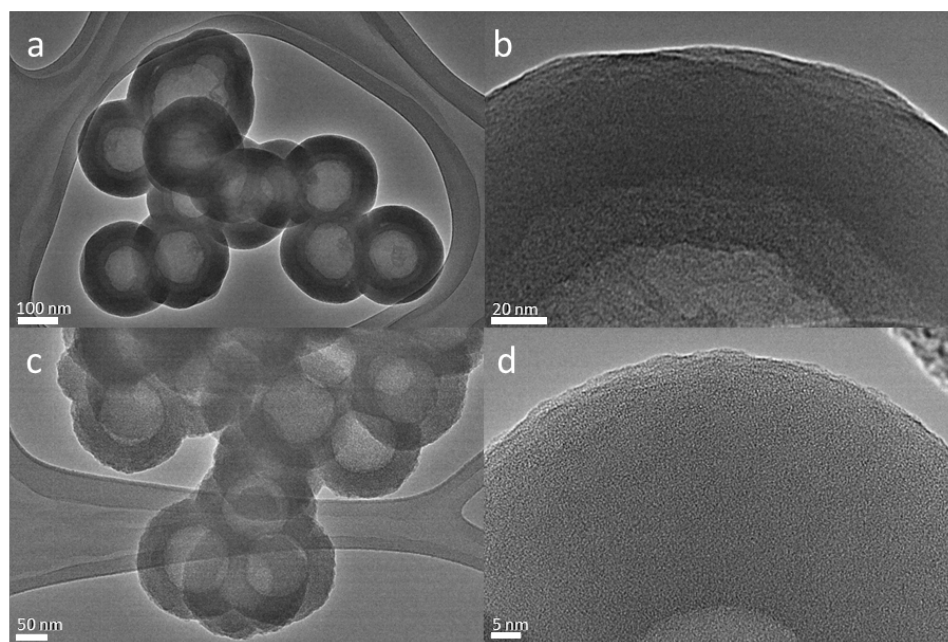


Figure 30 FTIR comparison of solid silica and mesoporous silica

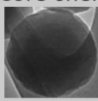
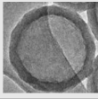
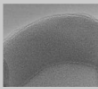
#### 4.3.4 Sealing of porous shell

A pore plugging strategy has been used to seal the porous shell after etching. The idea is to introduce TEOS molecules to the pores to form new silica structure within those pores (plugging). The mesoporous silica shell of the as prepared core-shell structure contains pores made from the long carbon chains of C<sub>18</sub>TMS. As a template, those surfactants occupy the pores and consequently make them unavailable for the TEOS molecules to diffuse in and condensed on. As a result, TEOS molecules form another outer shell on the existing mesoporous shell, as shown in Figure 31a and b. In order to maximize the heat storage material portion of the capsule, pore plugging sealing is more favorable than this two layered shell structure. A calcination process is performed to remove the surfactant and to make the pores available for TEOS “plugging”. In Figure 31c and d, there are no two layer structure on the shell can be distinguished by TEM, indicating successful pore plugging of the original mesoporous silica shell. Additionally, while thickness of the outer shell can be controlled by the amount of TEOS added, excessive solid silica particles might form if the parameters are not precisely controlled. Previous study shows that secondary nucleation will happen when the critical surface area of silica seeds in the dispersion is not reached. For the meantime, maintaining a relatively short distance between seeds and thus a short diffusion time for hydrolyzed TEOS monomers is also crucial to obtain monodispersed particles.<sup>21-23</sup>



*Figure 31 Pore-plug sealing of porous shell after etching*

The successful sealing is also verified by different pore volume of samples before and after sealing by a BET surface area analyzer. For instance, cumulative pore volume of core-shell silica, hollow porous silica after calcination (etched silica) and sealed hollow silica (sealed silica) are characterized using BJH method. The summarized result in Table 2 clearly shows that the sealed silica has significantly lower cumulative pore volume ( $0.008 \text{ cm}^3/\text{g}$ ) than that of as prepared core-shell silica ( $0.041 \text{ cm}^3/\text{g}$ ) and etched silica ( $0.035 \text{ cm}^3/\text{g}$ ), implying majority of the pores in the shell has been effectively “plugged” during the sealing process. It is also noticed that the etched silica has a slightly larger average pore size (11.0 nm) than core-shell silica (10.6 nm) which corresponds with Shi’s hypothesis of pores been opened up by etching.<sup>16</sup> In the meantime, the decreased cumulative pore volume observed for etched silica, compare to that of core-shell silica, can potentially be resulted from the further condensation of silica during the calcination process.

Sample	BJH Pore Volume (m <sup>3</sup> /g)	BJH Ave. Pore Size (nm)	BJH Surface Area of Pores (m <sup>2</sup> /g)
Core-shell 	0.041073	10.6046	15.4920
Etched 	0.035286	11.0323	14.307
Sealed 	0.008115	9.3137	3.485

*Table 2 BJH pore volume of silica nanoparticles*

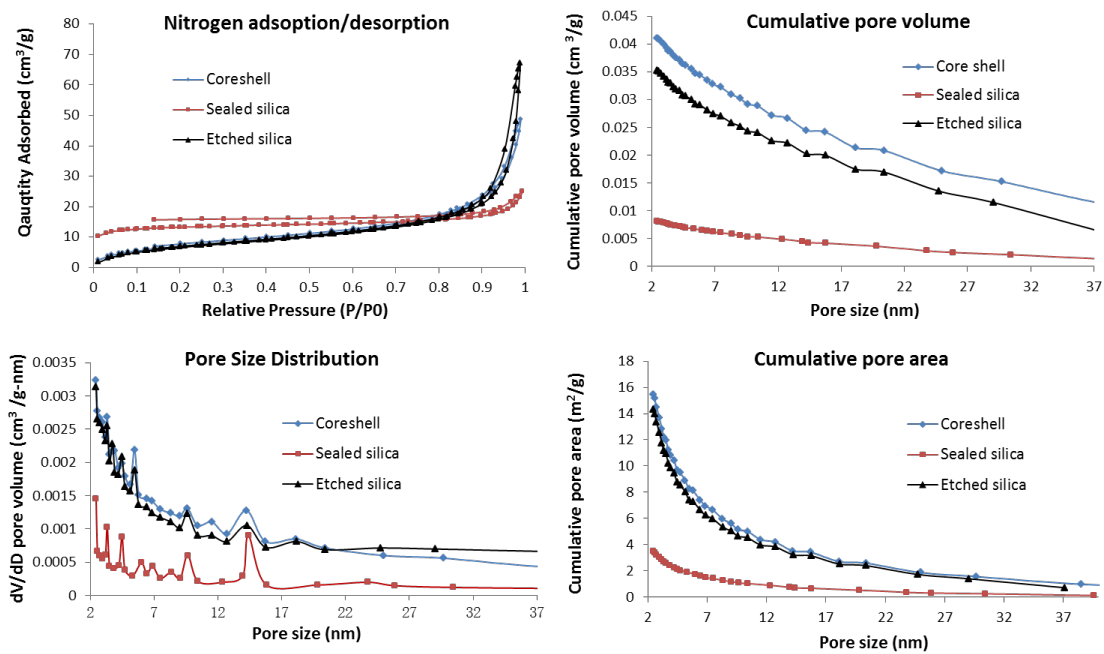
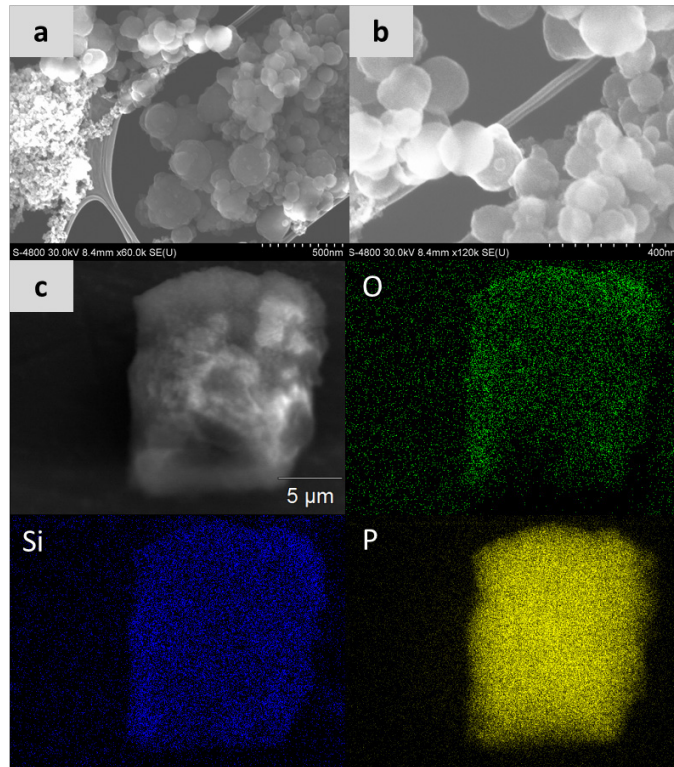


Figure 32 BET surface area analysis of silica nanoparticles

#### 4.4 Encapsulation of other materials

Silica nano-encapsulation technology can also be used for both organic and other inorganic materials. In Figure 33a and b, nano-encapsulation of stearic acid has been shown with excessive silica nanoparticles. Red phosphorous micro-encapsulation is also synthesized via the same silica coating method supported by its x-ray mapping of key elements (Figure 33c)



*Figure 33 Encapsulation of a&b) stearic acid and c) red phosphorous*



#### **4.5 Conclusion**

Versatility of the proposed silica coating method has been demonstrated in aforementioned encapsulation examples. Furthermore, the possible creation of void in micro/nano encapsulated PCM has been discussed and demonstrated by fabrication of hollow silica shell.

## **IV Final Conclusion**

### **1. Project Summary**

- A novel fabrication process is developed to synthesize the first ever microencapsulation of salt with high thermal stability and reliability
- Effect of particle size on fabrication process, thermal and rheological properties of microcapsules added HTF are analyzed
- Microencapsulated complex binary salt is demonstrated for the first time with proposed fabrication process
- Remarkable effective heat capacity enhancement obtained for different CSP configurations
- Versatility of encapsulation method is shown with organic, inorganic and metal encapsulation

A novel water-limited silica sol-gel coating process was used to achieve the first ever molten salt micro-encapsulation for high temperature thermal energy storage. The concept was first proven with a simple  $\text{KNO}_3@$ silica microcapsules. The encapsulation process was analyzed in detail using scanning electron microscopy (SEM), X-ray mapping, transmission electron microscopy (TEM), Fourier-transform infrared spectroscopy (FTIR). The process was shown to be precisely controllable, demonstrated by control of different encapsulation ratio and resulting shell thickness. The thermal properties were studied for said microcapsules showing shell stability and latent heat performance at relatively high temperatures (400°C).

The effect of effective capsule size on available latent heat and shell stability were investigated. The use of such PCM encapsulated microcapsules were then explored as additives in heat transfer fluid (HTF) for high temperature thermal energy storage, attempting for the first time, enhancement of HTF performance with latent heat as opposed to just increasing the specific heat.. Rheological property and thermal performance of  $\text{KNO}_3$ @silica microparticles added HTF (solar salt) were then analyzed with the highest effective heat capacity enhancement of 11% obtained.

The novel micro-encapsulation method developed in this work was then shown to effectively encapsulate composite binary salts displaying its capability to move from a single component to a more complex system. Binary carbonate salt microcapsules were encapsulated using the same method and characterized by the above mentioned tools. The high specific and latent heat capable binary salt microcapsules were added to HTF to obtain remarkable effective heat capacity improvement. Through the high specific heat and latent heat of the binary carbonate salt, remarkable 40.5% and 134.4% enhancement on effective heat capacity over the standard HTF (solar salt) was achieved for active and passive solar thermal systems respectively.

Finally, the versatility of the encapsulation method is demonstrated by micro/nano-encapsulation of different materials, ranging from organic compounds like stearic acid, metals like gallium (low melting point), stainless steel (very high melting point), to inorganic materials like phosphorous. The possibility of void creation, to accommodate large volumetric expansion during phase change, in MEPCM is also demonstrated, thus showing the versatile nature and great potential for the developed technique.

## **2. Future Work**

Several directions of high temperature MEPCM are particularly interesting to author. Primarily, to reach the goals for next generation thermal storage, continuous effort needs to be put in to increase the operating temperature and effective heat capacity of MEPCM. The can be done by encapsulating other binary or ternary molten salt or metal alloy. Secondly, more effort can be put into thermal stability analysis of silica at higher temperature. Also, void creation within MEPCM can be crucial to thermal stability improvement at higher temperature for some materials with high thermal expansion coefficient. Finally, with a high heat capacity, high temperature compatible MEPCM available, an alternative CSP design can be explored for better utilization of the MEPCM. Meanwhile, MEPCM can also be incorporated to different high temperature thermal storage applications.

## V References

1. H. Zhang, J. Baeyens, G. Cáceres, J. Degrève and Y. Lv, *Prog. Energy Combust. Sci.*, 2016, **53**, 1-40.
2. M. M. Kenisarin, *Renew. Sust. Energ. Rev.*, 2010, **14**, 955-970.
3. M. Graham, E. Shchukina, P. F. De Castro and D. Shchukin, *J. Mater. Chem. A*, 2016, **4**, 16906-16912.
4. A. Sharma, V. V. Tyagi, C. R. Chen and D. Buddhi, *Renew. Sust. Energ. Rev.*, 2009, **13**, 318-345.
5. T. Nomura, N. Sheng, C. Zhu, G. Saito, D. Hanzaki, T. Hiraki and T. Akiyama, *Appl. Energy*, 2017, **188**, 9-18.
6. T. Nomura, C. Zhu, N. Sheng, G. Saito and T. Akiyama, *Sci. Rep.*, 2015, **5**, 9117.
7. A. Mathur, R. Kasetty, J. Oxley, J. Mendez and K. Nithyanandam, *Energy Procedia*, 2014, **49**, 908-915.
8. W. Stöber, A. Fink and E. Bohn, *J. Colloid Interface Sci.*, 1968, **26**, 62-69.
9. N. R. Jankowski and F. P. McCluskey, *Appl. Energy*, 2014, **113**, 1525-1561.
10. H. Zhang, X. Wang and D. Wu, *J. Colloid Interface Sci.*, 2010, **343**, 246-255.
11. S. Liang, Q. Li, Y. Zhu, K. Chen, C. Tian, J. Wang and R. Bai, *Energy*, 2015, **93**, Part 2, 1684-1692.
12. S. Tahan Latibari, M. Mehrali, M. Mehrali, T. M. Indra Mahlia and H. S. Cornelis Metselaar, *Energy*, 2013, **61**, 664-672.
13. G. Fang, Z. Chen and H. Li, *Chem. Eng. J.*, 2010, **163**, 154-159.
14. Q. He, X. Cui, F. Cui, L. Guo and J. Shi, *Microporous Mesoporous Mater.*, 2009, **117**, 609-616.
15. Y. Chen, H. Chen, L. Guo, Q. He, F. Chen, J. Zhou, J. Feng and J. Shi, *ACS Nano*, 2010, **4**, 529-539.
16. Y. Chen, H. Chen, D. Zeng, Y. Tian, F. Chen, J. Feng and J. Shi, *ACS Nano*, 2010, **4**, 6001-6013.
17. A. R. Thompson and R. E. Vener, *Ind. Eng. Chem.*, 1948, **40**, 478-481.
18. C. J. Brinker, *J. Non-Cryst. Solids*, 1988, **100**, 31-50.

19. I. A. Ibrahim, A. Zikry and M. A. Sharaf, *J. Am. Sci.*, 2010, **6**, 985-989.
20. D. L. Green, S. Jayasundara, Y.-F. Lam and M. T. Harris, *J. Non-Cryst. Solids*, 2003, **315**, 166-179.
21. G. H. Bogush, M. A. Tracy and C. F. Zukoski, *J. Non-Cryst. Solids*, 1988, **104**, 95-106.
22. A. Van Blaaderen, J. Van Geest and A. Vrij, *J. Colloid Interface Sci.*, 1992, **154**, 481-501.
23. K.-S. Chou and C.-C. Chen, *Ceram. Int.*, 2008, **34**, 1623-1627.
24. R. Al-Oweini and H. El-Rassy, *J. Mol. Struct.*, 2009, **919**, 140-145.
25. J.-H. Liu, Y.-H. Zhang, L.-Y. Wang and Z.-F. Wei, *Spectrochim. Acta, Part A*, 2005, **61**, 893-899.
26. M. F. Z. Kadir, Z. Aspanut, S. R. Majid and A. K. Arof, *Spectrochim. Acta, Part A*, 2011, **78**, 1068-1074.
27. H. W. Sheng, K. Lu and E. Ma, *Acta Mater.*, 1998, **46**, 5195-5205.
28. Y. Hong, W. Wu, J. Hu, M. Zhang, A. A. Voevodin, L. Chow and M. Su, *Chem. Phys. Lett.*, 2011, **504**, 180-184.
29. F. Bernd and D. H. Kenneth, *Metrologia*, 2006, **43**, 71.
30. C. C. Koch, J. S. C. Jang and S. S. Gross, *J. Mater. Res.*, 1989, **4**, 557-564.
31. C. Hock, S. Straßburg, H. Haberland, B. v. Issendorff, A. Aguado and M. Schmidt, *Phys. Rev. Lett.*, 2008, **101**, 023401.
32. F. Spaepen and D. Turnbull, *Scr. Metall.*, 1979, **13**, 149-151.
33. M. Chieruzzi, A. Miliozzi, T. Crescenzi, L. Torre and J. M. Kenny, *Nanoscale Res. Lett.*, 2015, **10**, 273.
34. I. Rahman, P. Vejayakumaran, C. Sipaut, J. Ismail, M. A. Bakar, R. Adnan and C. Chee, *Colloids Surf., A*, 2007, **294**, 102-110.
35. Y. Yamagishi, H. Takeuchi, A. T. Pyatenko and N. Kayukawa, *AIChE J.*, 1999, **45**, 696-707.
36. F. Agyenim, N. Hewitt, P. Eames and M. Smyth, *Renew. Sust. Energ. Rev.*, 2010, **14**, 615-628.
37. M. Delgado, A. Lázaro, J. Mazo, J. M. Marín and B. Zalba, *Appl. Therm. Eng.*, 2012, **36**, 370-377.

38. L. Chen, T. Wang, Y. Zhao and X.-R. Zhang, *Energy Convers. Manage.*, 2014, **79**, 317-333.
39. T. Wang, L. Wang, L. Bai, G. Lin, X. Bu, X. Liu and G. Xie, *Energy Convers. Manage.*, 2015, **103**, 943-957.
40. Z. Qiu, X. Ma, P. Li, X. Zhao and A. Wright, *Renew. Sust. Energ. Rev.*, 2017, **77**, 246-262.
41. V. V. Tyagi, S. C. Kaushik, S. K. Tyagi and T. Akiyama, *Renew. Sust. Energ. Rev.*, 2011, **15**, 1373-1391.
42. M. Goel, S. K. Roy and S. Sengupta, *Int. J. Heat Mass Transfer*, 1994, **37**, 593-604.
43. X. Hu and Y. Zhang, *Int. J. Heat Mass Transfer*, 2002, **45**, 3163-3172.
44. R. Zeng, X. Wang, B. Chen, Y. Zhang, J. Niu, X. Wang and H. Di, *Appl. Energy*, 2009, **86**, 2661-2670.
45. R. Jacob and F. Bruno, *Renew. Sust. Energ. Rev.*, 2015, **48**, 79-87.
46. K. Vignarooban, X. Xu, A. Arvay, K. Hsu and A. M. Kannan, *Appl. Energy*, 2015, **146**, 383-396.
47. Y. Zheng, W. Zhao, J. C. Sabol, K. Tuzla, S. Neti, A. Oztekin and J. C. Chen, *Sol. Energy*, 2013, **87**, 117-126.
48. R. Fukahori, T. Nomura, C. Zhu, N. Sheng, N. Okinaka and T. Akiyama, *Appl. Energy*, 2016, **170**, 324-328.
49. A. Sarı, C. Alkan, D. Kahraman Döğüşcü and A. Biçer, *Sol. Energy Mater. Sol. Cells*, 2014, **126**, 42-50.
50. A. Sarı, C. Alkan, A. Biçer, A. Altuntaş and C. Bilgin, *Energy Convers. Manage.*, 2014, **86**, 614-621.
51. J. Huang, T. Wang, P. Zhu and J. Xiao, *Thermochim. Acta*, 2013, **557**, 1-6.
52. L. Cao, F. Tang and G. Fang, *Energy Build.*, 2014, **72**, 31-37.
53. F. Khakzad, Z. Alinejad, A. R. Shirin-Abadi, M. Ghasemi and A. R. Mahdavian, *Colloid. Polym. Sci.*, 2013, **292**, 355-368.
54. F. Yu, Z.-H. Chen and X.-R. Zeng, *Colloid. Polym. Sci.*, 2009, **287**, 549-560.
55. J. Pereira da Cunha and P. Eames, *Appl. Energy*, 2016, **177**, 227-238.
56. T. Do, Y. G. Ko, Y. Chun and U. S. Choi, *ACS Sustainable Chem. Eng.*, 2015, **3**, 2874-2881.

57. S. Ye, Q. Zhang, D. Hu and J. Feng, *J. Mater. Chem. A*, 2015, **3**, 4018-4025.
58. D. Platte, U. Helbig, R. Houbertz and G. SEXTL, *Macromol. Mater. Eng.*, 2013, **298**, 67-77.
59. F. Khakzad, Z. Alinejad, A. R. Shirin-Abadi, M. Ghasemi and A. R. Mahdavian, *Colloid. Polym. Sci.*, 2014, **292**, 355-368.
60. Y. Fang, H. Yu, W. Wan, X. Gao and Z. Zhang, *Energy Convers. Manage.*, 2013, **76**, 430-436.
61. K. Tumirah, M. Z. Hussein, Z. Zulkarnain and R. Rafeadah, *Energy*, 2014, **66**, 881-890.
62. X. Hu, Z. Huang and Y. Zhang, *Carbohydr. Polym.*, 2014, **101**, 83-88.
63. G. Fang, H. Li, F. Yang, X. Liu and S. Wu, *Chem. Eng. J.*, 2009, **153**, 217-221.
64. Z.-H. Chen, F. Yu, X.-R. Zeng and Z.-G. Zhang, *Appl. Energy*, 2012, **91**, 7-12.
65. Y. Fang, X. Liu, X. Liang, H. Liu, X. Gao and Z. Zhang, *Appl. Energy*, 2014, **132**, 551-556.
66. C. Liu, Z. Rao, J. Zhao, Y. Huo and Y. Li, *Nano Energy*, 2015, **13**, 814-826.
67. C. Chen, Z. Chen, X. Zeng, X. Fang and Z. Zhang, *Colloid. Polym. Sci.*, 2011, **290**, 307-314.
68. S. Lai, J. Carlsson and L. Allen, *Appl. Phys. Lett.*, 1998, **72**, 1098-1100.
69. M. Zhang, M. Y. Efremov, F. Schiettekatte, E. Olson, A. Kwan, S. Lai, T. Wisleder, J. Greene and L. Allen, *Phys. Rev. B*, 2000, **62**, 10548.
70. S. Lai, J. Guo, V. Petrova, G. Ramanath and L. Allen, *Phys. Rev. Lett.*, 1996, **77**, 99.
71. H. Jiang, K.-s. Moon, H. Dong, F. Hua and C. P. Wong, *Chem. Phys. Lett.*, 2006, **429**, 492-496.
72. H. Ribera and T. Myers, *Microfluidics and Nanofluidics*, 2016, **20**, 147.
73. E. Olson, M. Y. Efremov, M. Zhang, Z. Zhang and L. Allen, *J. Appl. Phys.*, 2005, **97**, 034304.
74. B. Dudda and D. Shin, *International Journal of Thermal Sciences*, 2013, **69**, 37-42.
75. H. Tiznobaik and D. Shin, *Appl. Phys. Lett.*, 2013, **102**, 173906.
76. M. K. Ram, P. D. Myers, C. Jotshi, D. Y. Goswami, E. K. Stefanakos, K. D. Arvanitis, E. Papanicolaou and V. Belessiotis, *International Journal of Energy Research*, 2017, **41**, 252-262.



77. M.-C. Lu and C.-H. Huang, *Nanoscale Res. Lett.*, 2013, **8**, 292.
78. H. Tiznobaik and D. Shin, *Int. J. Heat Mass Transfer*, 2013, **57**, 542-548.
79. R. S. Vajjha and D. K. Das, *Int. J. Heat Mass Transfer*, 2012, **55**, 4063-4078.
80. G. H. Zhang and C. Y. Zhao, *Renewable Energy*, 2011, **36**, 2959-2966.
81. B. Jo and D. Banerjee, *Mater. Lett.*, 2014, **122**, 212-215.
82. M. N. A. Hawlader, M. S. Uddin and M. M. Khin, *Appl. Energy*, 2003, **74**, 195-202.
83. A. Jamekhorshid, S. M. Sadrameli and M. Farid, *Renew. Sust. Energ. Rev.*, 2014, **31**, 531-542.
84. L. F. Cabeza, C. Castellón, M. Nogués, M. Medrano, R. Leppers and O. Zubillaga, *Energy Build.*, 2007, **39**, 113-119.
85. A. M. Khudhair and M. M. Farid, *Energy Convers. Manage.*, 2004, **45**, 263-275.
86. L. F. Cabeza, A. Castell, C. Barreneche, A. de Gracia and A. I. Fernández, *Renew. Sust. Energ. Rev.*, 2011, **15**, 1675-1695.
87. M. W. Chase, S. National Institute of and Technology, *NIST-JANAF thermochemical tables*, American Chemical Society ; American Institute of Physics for the National Institute of Standards and Technology, [Washington, D.C.]; Woodbury, N.Y., 1998.
88. D. Shin and D. Banerjee, *The International Journal of Structural Changes in Solids*, 2010, **2**, 25-31.
89. G. J. JANZ and M. R. LORENZ, *J. Chem. Eng. Data*, 1961, **6**, 321-323.
90. Z. S. Nickolov, O. Ozcan and J. D. Miller, *Colloids and Surfaces A: Physicochemical and Engineering Aspects*, 2003, **224**, 231-239.
91. S. Gunasekaran, G. Anbalagan and S. Pandi, *J. Raman Spectrosc.*, 2006, **37**, 892-899.
92. R. L. Lehman, J. S. Gentry and N. G. Glumac, *Thermochim. Acta*, 1998, **316**, 1-9.
93. P. Gimenez and S. Fereres, *Energy Procedia*, 2015, **69**, 654-662.
94. S. Haukka and A. Root, *The Journal of Physical Chemistry*, 1994, **98**, 1695-1703.
95. N. Sheela, S. Muthu and S. S. Krishnan, *Asian J. Chem.*, 2010, **22**, 5049.
96. D. L. Ou and A. B. Seddon, *J. Non-Cryst. Solids*, 1997, **210**, 187-203.
97. M. I. Loría-Bastarrachea, W. Herrera-Kao, J. V. Cauich-Rodríguez, J. M. Cervantes-Uc, H. Vázquez-Torres and A. Ávila-Ortega, *J. Therm. Anal. Calorim.*, 2011, **104**, 737-742.

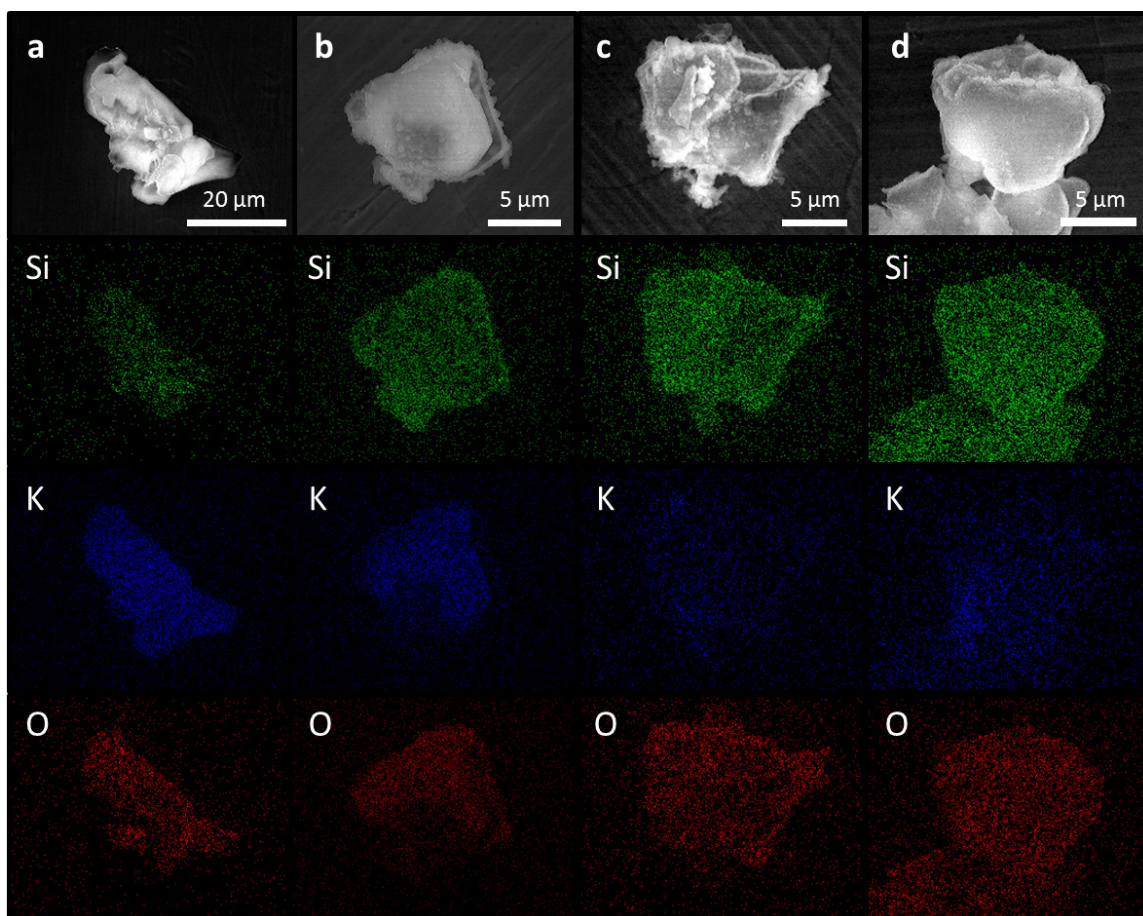
98. A. Gil, M. Medrano, I. Martorell, A. Lázaro, P. Dolado, B. Zalba and L. F. Cabeza, *Renew. Sust. Energ. Rev.*, 2010, **14**, 31-55.
99. M. Liu, N. H. Steven Tay, S. Bell, M. Belusko, R. Jacob, G. Will, W. Saman and F. Bruno, *Renew. Sust. Energ. Rev.*, 2016, **53**, 1411-1432.
100. S. Kuravi, J. Trahan, D. Y. Goswami, M. M. Rahman and E. K. Stefanakos, *Prog. Energy Combust. Sci.*, 2013, **39**, 285-319.
101. Q. Peng, J. Ding, X. Wei and G. Jiang, *Energy Procedia*, 2017, **105**, 4420-4427.
102. R. Tamme, 2007.
103. K. Nithyanandam, R. Pitchumani and A. Mathur, *Appl. Energy*, 2014, **113**, 1446-1460.
104. K.-C. Kao, C.-J. Tsou and C.-Y. Mou, *Chem. Commun.*, 2012, **48**, 3454-3456.
105. Z. Sun and Y. Luo, *Soft Matter*, 2011, **7**, 871-875.
106. C. A. García-González, M. C. Camino-Rey, M. Alnaief, C. Zetzl and I. Smirnova, *The Journal of Supercritical Fluids*, 2012, **66**, 297-306.
107. T. Zhang, J. Ge, Y. Hu, Q. Zhang, S. Aloni and Y. Yin, *Angew. Chem.*, 2008, **120**, 5890-5895.
108. H. Zhu, Y. Ma, Y. Fan and J. Shen, *Thin Solid Films*, 2001, **397**, 95-101.

## VI Appendix

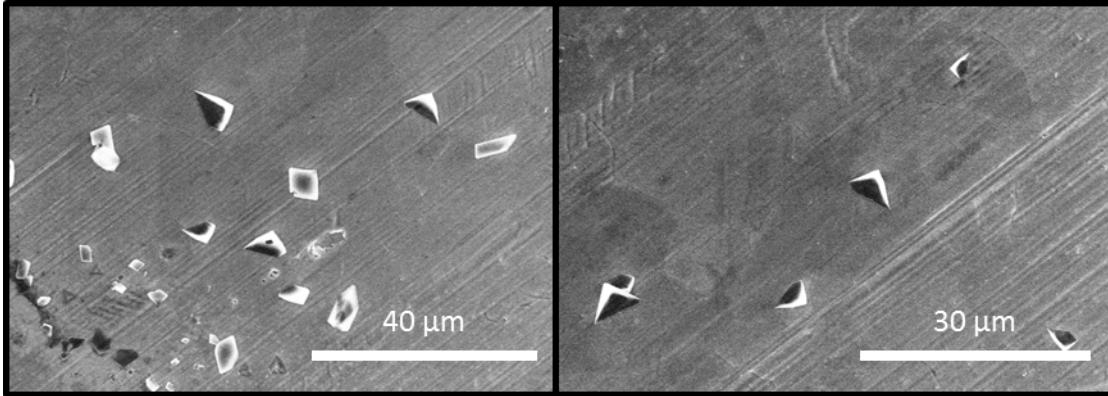
### 1. List of Appendix

Appendix 1 X-Ray mapping of a) S-0.75;b) S-1; c) S-1.5 and d) S-2 after 10 cycles of DSC test. Potassium is more difficult to be detected at higher encapsulation ratios due to thicker silica coating.....	109
Appendix 2 S-0.5 sample after 10 cycles of DSC test. Capsule is broken and recrystallized salt crystal is observed.....	110
Appendix 3 Melting peak comparison of S-0.5 and S-0.75 on 10 cycles DSC results. S-0.5 clearly shows a changing of latent heat while S-0.75 stays the almost the same .....	111
Appendix 4 10 cycle DSC result of $\text{KNO}_3$ and samples with different TEOS concentration ....	112
Appendix 5 TEM image of S-0.5 after sonication in water .....	113
Appendix 6 Photo of different samples after DSC test. Pure salt sticks on the wall of DSC Pan. S-0.5 sample forms hard solid paste, while other samples remain as powder.....	114
Appendix 7 Photo of binary salt and HTF mixture samples after DSC.....	115
Appendix 8 Heat flow data of $\text{LiNa@Si}$ and SS 20% mixture.....	116
Appendix 9 Heat flow data of pure solar salt .....	117
Appendix 10 A sequence of SEM images shows salt deformation under electron beam. X-ray mapping shows clear core-shell structure of a broken shell caused by salt deformation .....	118

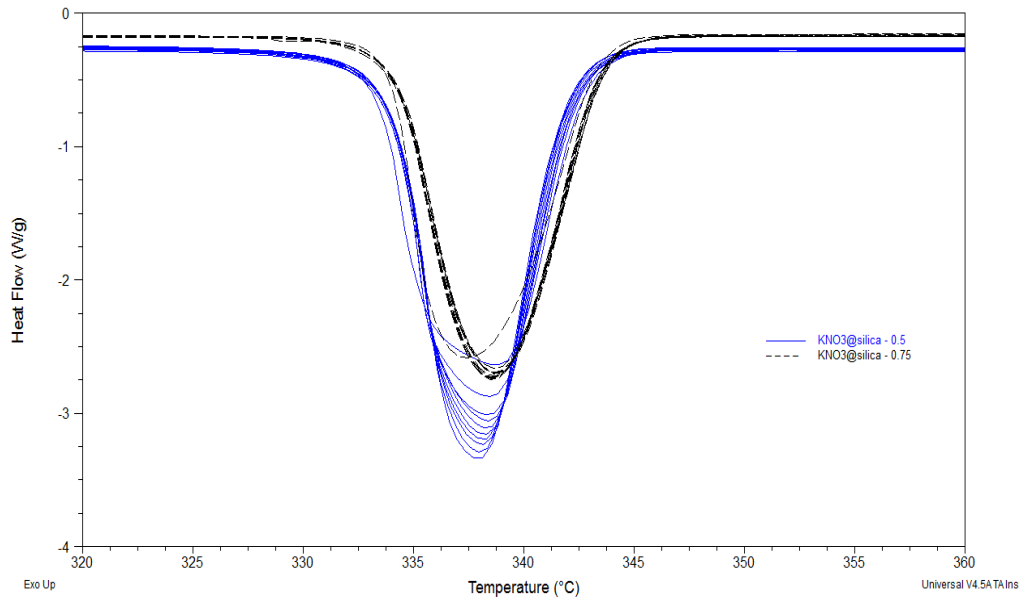
Appendix 11 10 cycles DSC data of LiNa@Si-1.5 (top left), pure LiNa binary carbonate (top right) , LiK@Si-1.5 (bottom left) pure LiK binary carbonate (bottom right)..... 119



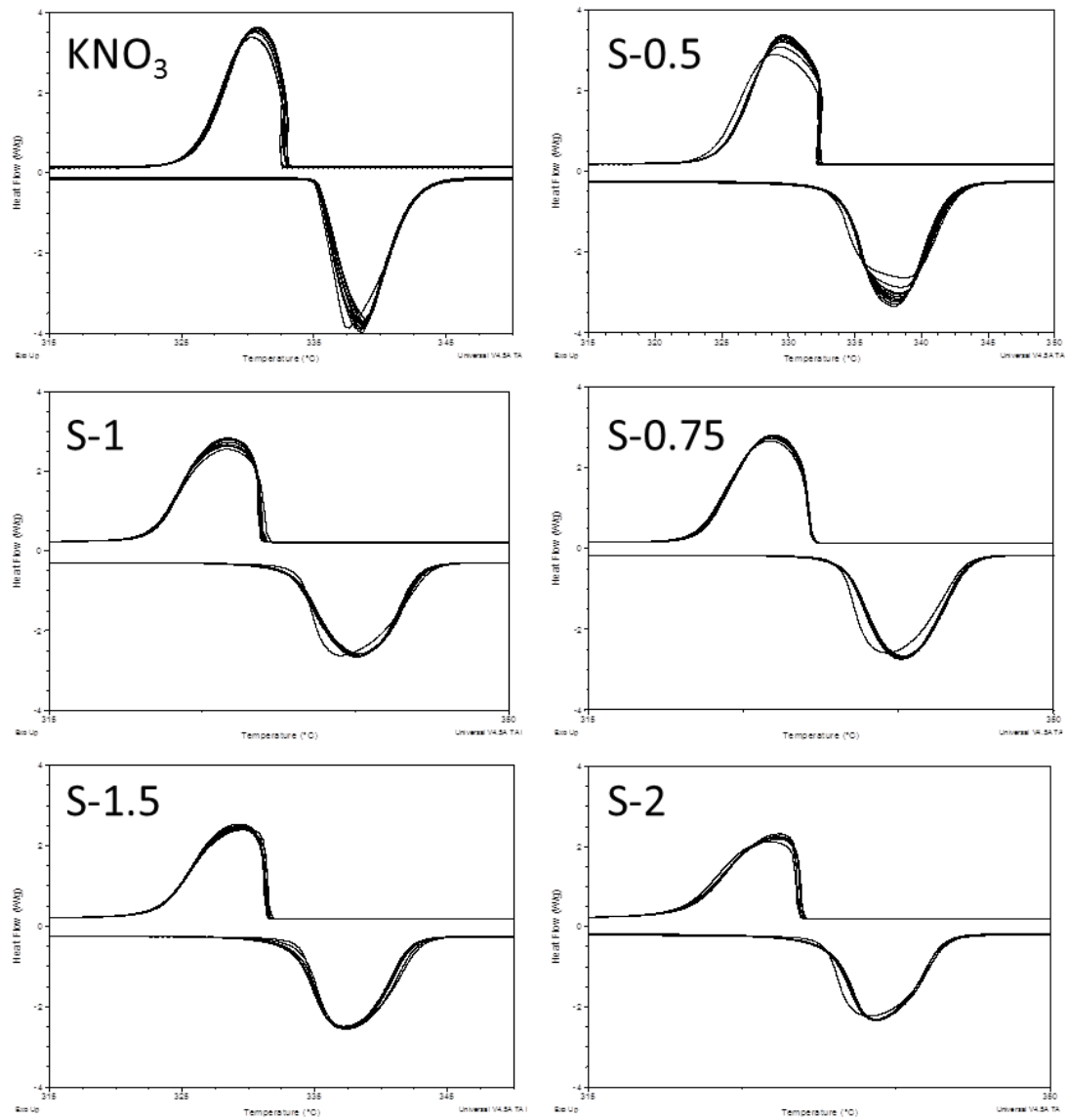
*Appendix 1 X-Ray mapping of a) S-0.75; b) S-1; c) S-1.5 and d) S-2 after 10 cycles of DSC test. Potassium is more difficult to be detected at higher encapsulation ratios due to thicker silica coating*



*Appendix 2 S-0.5 sample after 10 cycles of DSC test. Capsule is broken and recrystallized  
salt crystal is observed*

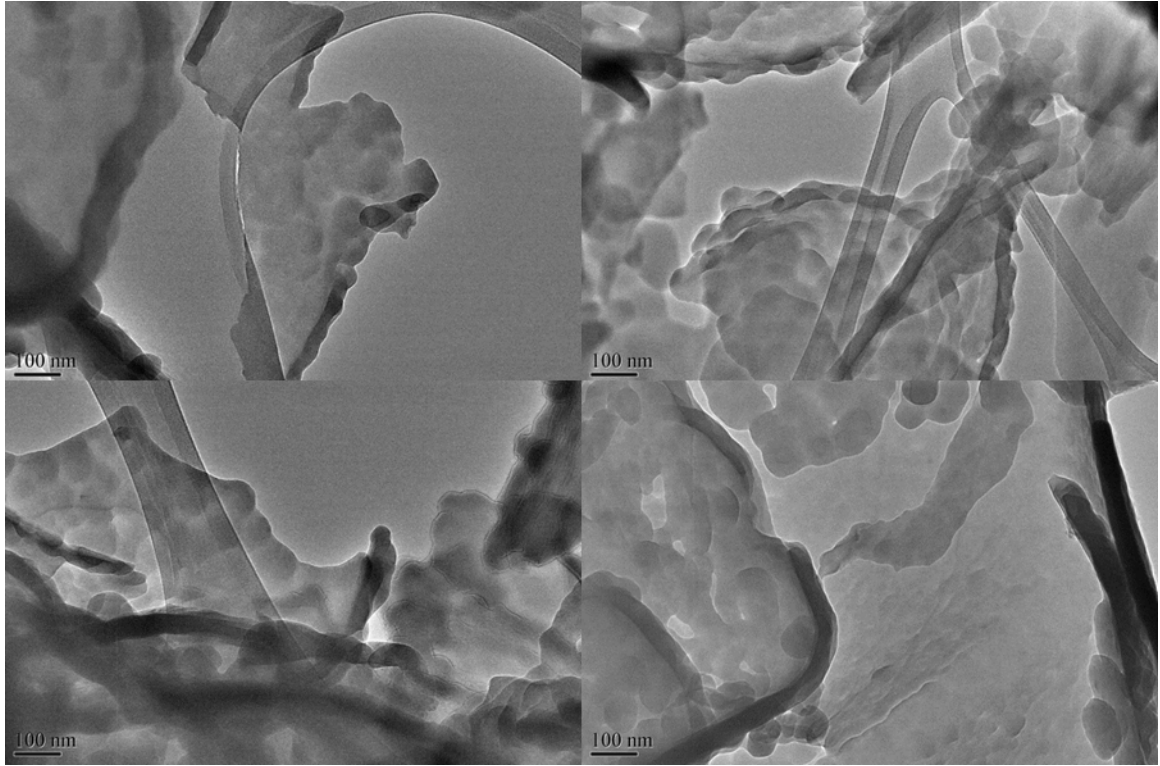


*Appendix 3 Melting peak comparison of S-0.5 and S-0.75 on 10 cycles DSC results. S-0.5 clearly shows a changing of latent heat while S-0.75 stays the almost the same*

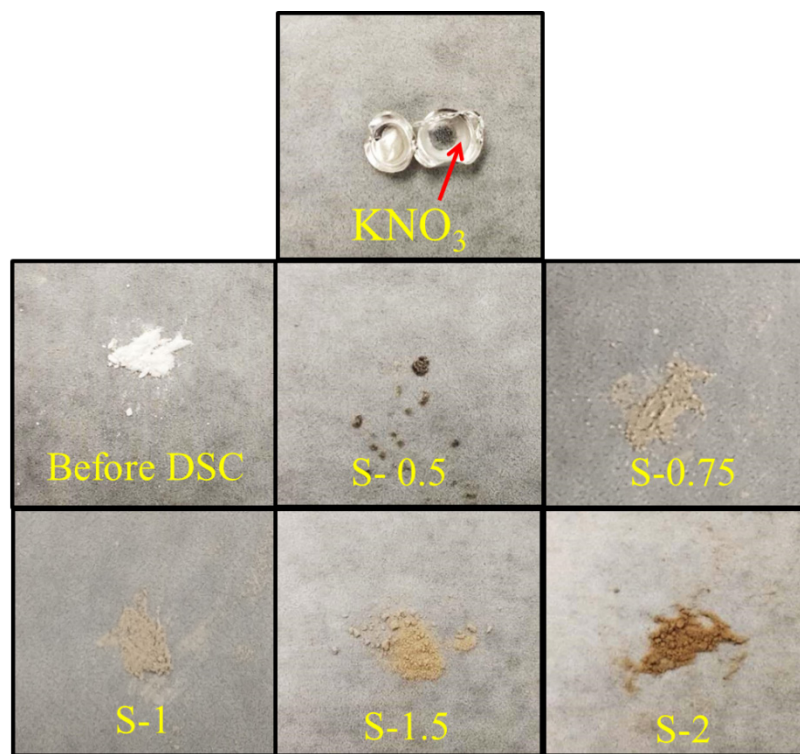


*Appendix 4 10 cycle DSC result of KNO<sub>3</sub> and samples with different TEOS concentration*





*Appendix 5 TEM image of S-0.5 after sonication in water*

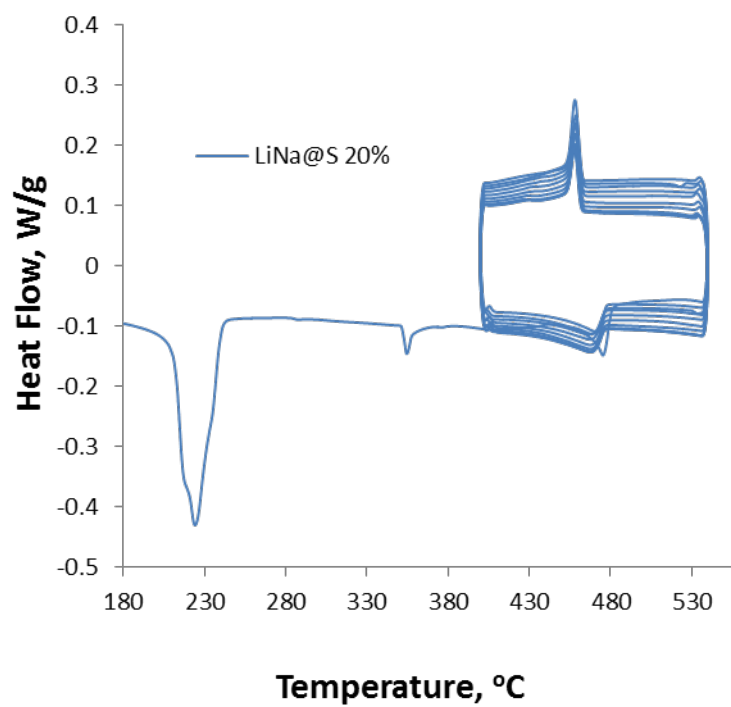


*Appendix 6 Photo of different samples after DSC test. Pure salt sticks on the wall of DSC*

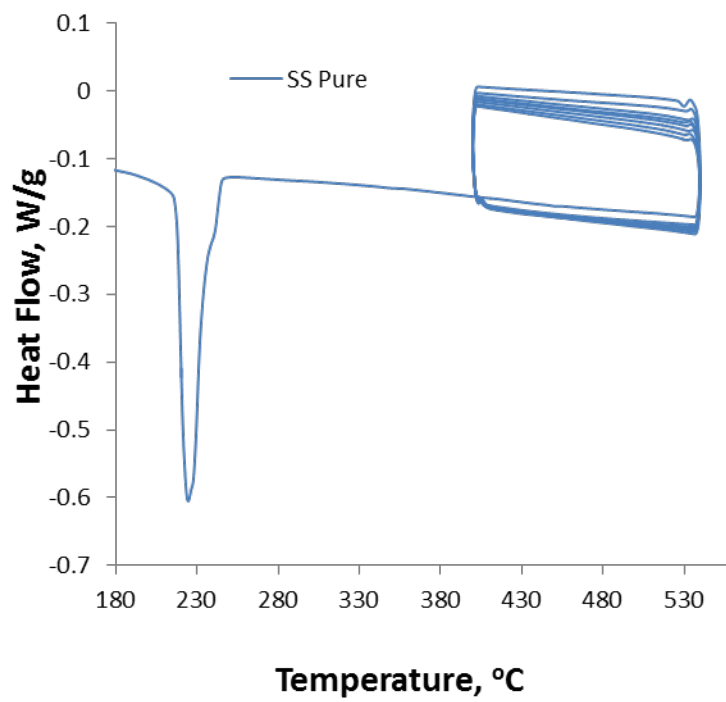
*Pan. S-0.5 sample forms hard solid paste, while other samples remain as powder*



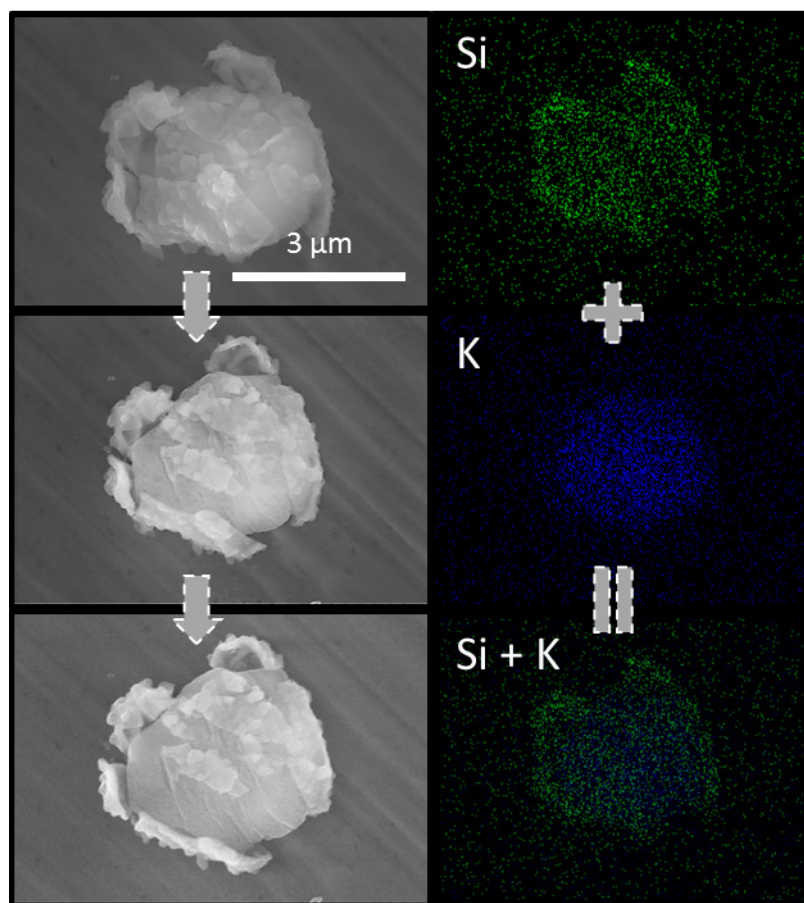
*Appendix 7 Photo of binary salt and HTF mixture samples after DSC*



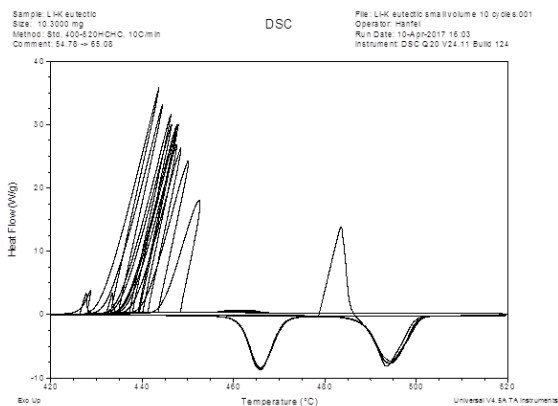
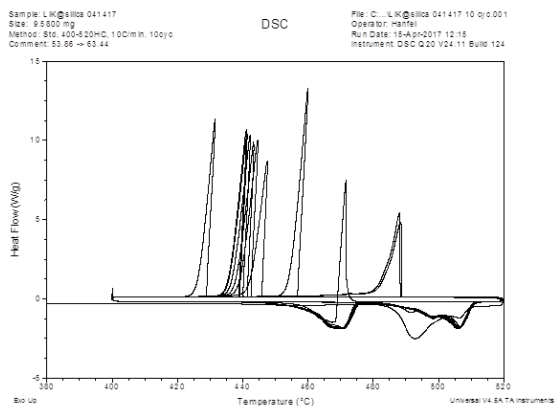
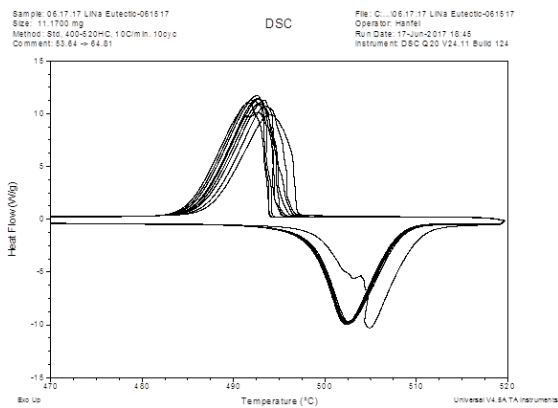
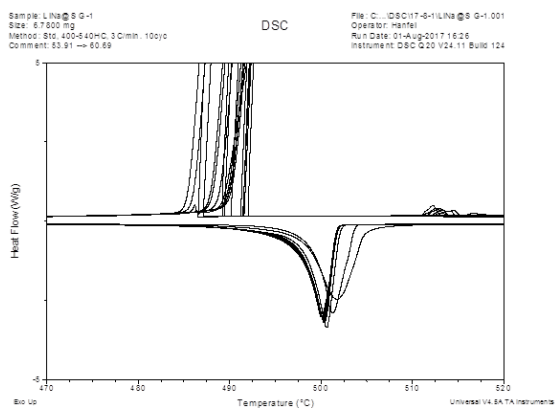
*Appendix 8 Heat flow date of LiNa@Si and SS 20% mixture*



*Appendix 9 Heat flow data of pure solar salt*



*Appendix 10 A sequence of SEM images shows salt deformation under electron beam. X-ray mapping shows clear core-shell structure of a broken shell caused by salt deformation*



*Appendix 11 10 cycles DSC data of LiNa@Si-1.5 (top left), pure LiNa binary carbonate (top right), LiK@Si-1.5 (bottom left) pure LiK binary carbonate (bottom right)*